

A Systematic Analysis of Out-of-Distribution Detection Under Representation and Training Paradigm Shifts

C. César Claros Olivares

Electrical & Computer Engineering
University of Delaware

Abstract

We present a systematic comparison of out-of-distribution (OOD) detection methods across CLIP-stratified regimes using AURC and AUGRC as primary metrics. Experiments cover two representation paradigms: CNNs trained from scratch and a fine-tuned Vision Transformer (ViT), evaluated on CIFAR-10/100, SuperCIFAR-100, and TinyImageNet. Using a multiple-comparison-controlled, rank-based pipeline (Friedman test with Conover–Holm post-hoc) and Bron–Kerbosch cliques, we find that the learned feature space largely determines OOD efficacy. For both CNNs and ViTs, probabilistic scores (e.g., MSR, GEN) dominate misclassification (ID) detection. Under stronger shifts, geometry-aware scores (e.g., NNGuide, fDBD, CTM) prevail on CNNs, whereas on ViTs GradNorm and KPCA Reconstruction Error remain consistently competitive. We further show a class-count–dependent trade-off for Monte-Carlo Dropout (MCD) and that a simple PCA projection improves several detectors. These results support a representation-centric view of OOD detection and provide statistically grounded guidance for method selection under distribution shift. Code is available at https://anonymous.4open.science/r/ood_systematic-C990/

1 Introduction

In recent years, there has been a significant increase in approaches dealing with out-of-distribution (OOD) detection (Ammar et al., 2023; Bibas et al., 2021; Hendrycks and Gimpel, 2016; Hendrycks et al., 2019; Huang et al., 2021; Lee et al., 2018; Liu and Qin, 2023; Liu et al., 2020, 2023; Ngoc-Hieu et al., 2023; Park

Austin J. Brockmeier

Electrical & Computer Engineering
University of Delaware

et al., 2023; Wang et al., 2022) given their relevance in the reliable deployment of deep learning models, particularly in safety-critical applications. A significant vulnerability of deep neural networks (DNNs) is their tendency to produce *silent failures* (Jaeger et al., 2022; Traub et al., 2024), which are conceptualized as incorrect predictions with high confidence that are hard to detect. A reliable DNN classifier should not only accurately classify known in-distribution (ID) samples, but also effectively flag OOD inputs as *unknown*. However, most of these OOD detection methods show inconsistent behavior for different data sets.

For instance, the widely used maximum softmax response (MSR) (Hendrycks and Gimpel, 2016), a strong baseline for small-scale OOD detection, does not scale well to challenging conditions presented by large datasets such as ImageNet-1k (Deng et al., 2009). Hendrycks et al. (2019) hypothesizes that in datasets with many visually similar classes, a classifier might produce low softmax confidence for a legitimate ID image not due to unfamiliarity, but because the precise class is difficult to determine, dispersing the probability mass. This issue makes MSR problematic for large-scale detection. In contrast, the maximum logit score (MLS) (Hendrycks et al., 2019), which uses the negative of the maximum unnormalized logit, was proposed as a better baseline for large-scale OOD detection. Experiments showed that MLS significantly outperforms MSR in large-scale data sets, with improvements over 10% AUROC in some cases, whereas the difference was minor on small-scale CIFAR-10. This highlights a crucial inconsistency in method performance as the number of training classes increases.

Furthermore, some methods that performed well in small-scale settings, such as the Mahalanobis distance (Lee et al., 2018), encountered numerical problems when scaled to 1000 classes (Hendrycks et al., 2019). Mahalanobis distance utilizes a mixture of class-conditional Gaussians on features to identify OOD samples, showing effectiveness on datasets like CIFAR-10. However, its scaling issues underscore that

methods that rely on specific feature space properties derived from training data can become unstable or computationally challenging with a large number of classes. In addition, the observation that methods that are effective in natural images might differ from those for other data types, such as medical images (Gutbrod et al., 2025), where feature-based methods might excel, also subtly suggests that data scale and complexity, often correlated with the number of classes, influence the effectiveness of the method.

By contrasting multiple OOD detection methods and performance metrics obtained using CIFAR-10, CIFAR-100 (including superclasses) and TinyImagenet as ID datasets evaluated in near, mid and far OOD scenarios, we highlight the varying effectiveness of methods across different scales and the need for approaches specifically designed or validated depending on the number of classes in the training set.

2 Related Work

The inconsistencies in OOD evaluation have spurred multiple benchmarking efforts to standardize procedures and report more comprehensive results. However, in general, the impact of the number of classes in the training set has been overlooked.

Yang et al. (2022), for example, presents an extensive and unified benchmark framework designed to evaluate and compare out-of-distribution (OOD) detection methods across neighboring fields, including anomaly detection (AD), open set recognition (OSR), and model uncertainty estimation. Furthermore, the authors implement a codebase named *OpenOOD*, which integrates multiple OOD detection methods and evaluates them in a generalized OOD detection framework using 9 designed benchmarks and 4 OOD detection datasets that include MNIST, CIFAR-10, CIFAR-100, and ImageNet. Each benchmark features near-OOD (semantic shifts) and far-OOD (domain shifts) scenarios and reports AUROC, FPR@95, and AUPR as metrics. Specifically, they show that the best performing OOD detection methods between CIFAR-10 and CIFAR-100, considering near- and far-OOD scenarios, are not the same. Also, the authors state that despite ImageNet’s higher complexity, ImageNet-based benchmarks sometimes yield higher OOD detection performance than CIFAR-10/100. In a follow-up work, Zhang et al. (2023) extended *OpenOOD*’s codebase, implementing more OOD detection methods and extending its evaluation capabilities to larger datasets and recent foundation models. Although both studies experiment with multiple datasets with an increasing number of classes, they do not explore the impact that the number of classes in the training sets has on the

OOD detection performance. Additionally, this work does not consider some OOD detection methods that exploit geometric properties in the feature space such as NNGuide (Park et al., 2023), fLBD (Liu and Qin, 2023) or CTM (Ngoc-Hieu et al., 2023).

In a more theoretically grounded effort, Jaeger et al. (2022) identifies that conceptually similar problems such as misclassification detection, OOD detection, selective classification, and uncertainty quantification have heterogeneous task definitions and incompatible benchmarks. Accordingly, this work advocates for a unified evaluation framework centered on failure detection using confidence scoring functions (CSFs), with the Area Under the Risk-Coverage Curve (AURC) (Geifman et al., 2018) providing a holistic metric. An associated codebase, coined *FD-Shifts*, benchmarks a suite of CSFs across multiple datasets that include CAMELYON-17-Wilds, iWildCam-2020-Wilds, BREEDS-ENTITY-13, CIFAR-10/100, and TinyImagenet while also considering different failure types, including covariate shifts (e.g., sub-class and corruption shifts) and new-class shifts (e.g., semantic and non-semantic shifts). More specifically, Jaeger et al. (2022) report that Max-Softmax Response (MSR) consistently outperformed more sophisticated methods on most distribution shifts except non-semantic new-class shifts, where OOD detection methods performed better. Traub et al. (2024), however, argued that the reliance of the AURC on selective risk at fixed thresholds does not adequately reflect holistic system performance. In response, they introduce a novel metric, the Area Under the Generalized Risk-Coverage Curve (AUGRC), which aggregates misclassification risk across all thresholds and better captures the joint probability of failure and its acceptance, fixing the limitations of the AURC. Both studies evaluate CIFAR-10 and CIFAR-100, considering multiple distribution shifts, but do not identify any dependence of the OOD detection performance on the number of classes in the training sets.

In a more applied setting, Bungert et al. (2023) explore *silent failures* in the classification of medical images. The authors benchmark various CSFs under realistic distribution shifts such as corruption (e.g. noise), acquisition (e.g. multiple data sources), and manifestation (e.g. unseen forms of a pathology) shifts. This study builds four biomedical imaging datasets, combining in some cases multiple sources, including dermoscopy, chest radiograph, fluorescence microscopy, and CT of lung nodules. This study highlights that none of the advanced CSFs obtained from different selective classification approaches such as DeepGamblers (Liu et al., 2019), ConfidNet (Corbière et al., 2019; Corbière et al., 2021), or Monte Carlo

Dropout (Gal and Ghahramani, 2016) (MCD) variants (CSFs obtained from predictions generated by MCD activated at inference time) consistently outperform the MSR baseline. Although MCD-MSR performs best on average, results vary significantly depending on the data set and the type of shift, revealing trade-offs. In other words, this work emphasizes that a CSF that performs well under one domain shift may perform poorly under another. This highlights the difficulty in developing CSFs that generalize reliably in diverse biomedical conditions. Moreover, the choice of AURC as the main in this study may have hidden some trends in the performance of the CSFs.

Also in the medical domain, Gutbrod et al. (2025) introduce a domain-specific benchmarking suite designed to evaluate OOD detection in medical imaging, called *OpenMIBOOD*. The authors construct three distinct benchmarks: MIDOG (histopathology), PhaKIR (endoscopy), and OASIS-3 (MRI), spanning a total of 14 datasets, each stratified into in-distribution (ID), covariate-shifted ID (cs-ID), near-OOD and far-OOD categories. They evaluated 24 post-hoc OOD detection methods, including classification-based, feature-based, and hybrid approaches, using standard metrics such as AUROC, FPR@95, and the harmonic mean of AUPR-IN and AUPR-OUT. The results reveal that methods effective on natural image benchmarks often fail in medical domains, with feature-based approaches outperforming probabilistic-based approaches across most scenarios. The authors highlight that covariate shift detection is more tractable than semantic shift detection in medical imaging. Furthermore, methods such as Residual and ViM (Wang et al., 2022), while successful on natural image benchmarks, exhibit inconsistent performance in medical data sets. A key insight is that medical imaging tasks often involve lower data variance and fewer classes, favoring methods that exploit deep feature representations over those that rely on probabilistic predictions.

3 Methods

3.1 Definitions and Notations

We consider a supervised classification problem where each input sample is denoted by $\mathbf{x} \in \mathcal{X}$, and its corresponding label is $y \in \mathcal{Y} = \{1, \dots, C\}$, representing one of C possible classes. The label can also be represented in one-hot encoding as $\mathbf{y} = [\delta_y(1), \dots, \delta_y(C)]$, where $\delta_y(c) = \begin{cases} 1 & y = c \\ 0 & y \neq c \end{cases}$. The training dataset is defined as $\mathcal{D}_{\text{train}} = \{(\mathbf{x}_i, y_i)\}_{i=1}^{N_{\text{train}}}$, the test set as $\mathcal{D}_{\text{test}} = \{(\mathbf{x}_i^{\text{test}}, y_i^{\text{test}})\}_{i=1}^{N_{\text{test}}}$, and an out-of-distribution

(OOD) dataset as $\mathcal{D}_{\text{OOD}} = \{(\mathbf{x}_i^{\text{OOD}}, 0)\}_{i=1}^{N_{\text{OOD}}}$, which contains samples not belonging to any of the known classes. For a given class $c \in \mathcal{Y}$, we define the subset of data corresponding to that class within a set \mathcal{D} as $\mathcal{D}^c = \{(\mathbf{x}, y) \in \mathcal{D} \mid y = c\}$, with cardinality $N^c = |\mathcal{D}^c|$.

We denote the classifier as a neural network function $f : \mathcal{X} \rightarrow \mathbb{R}^C$ parameterized by weights and biases $\mathbf{W} = \{(\mathbf{W}_1, \mathbf{b}_1), \dots, (\mathbf{W}_L, \mathbf{b}_L)\}$. This model is decomposed into an encoder $h : \mathcal{X} \rightarrow \mathbb{R}^D$, defined by layers up to $L-1$, and a linear classifier head $g : \mathbb{R}^D \rightarrow \mathbb{R}^C$ parametrized by the weights in the L -th layer. The complete model is composed as $f(\mathbf{x}) = (g \circ h)(\mathbf{x})$. For a given input \mathbf{x} , the penultimate-layer representation is $\mathbf{h} = h(\mathbf{x}) \in \mathbb{R}^D$, and the classifier outputs a logit vector via $g(\mathbf{h}) = \mathbf{W}_L \mathbf{h} + \mathbf{b}_L$, where $\mathbf{W}_L = [\mathbf{w}_{1L}, \dots, \mathbf{w}_{CL}] \in \mathbb{R}^{C \times D}$ and $\mathbf{b}_L = [b_{1L}, \dots, b_{CL}] \in \mathbb{R}^C$. The predicted class is $m(\mathbf{x}) = \arg \max_c [f(\mathbf{x})]_c$, and the softmax-based class probabilities are given by $p(\mathbf{x}) = \mathbf{p} = \left[\frac{\exp(f(\mathbf{x})_1)}{\sum_j \exp(f(\mathbf{x})_j)}, \dots, \frac{\exp(f(\mathbf{x})_C)}{\sum_j \exp(f(\mathbf{x})_j)} \right]$.

We define the matrix of penultimate-layer activations for a dataset \mathcal{D} of size N as $\mathbf{H} = [\mathbf{h}_1, \dots, \mathbf{h}_N]^\top \in \mathbb{R}^{N \times D}$, and the corresponding matrix for class c as $\mathbf{H}^c = [\mathbf{h} : \mathbf{x} \in \mathcal{D}^c]^\top \in \mathbb{R}^{N^c \times D}$. The global mean of the features is $\boldsymbol{\mu} = \frac{1}{N} \sum_{1 \leq i \leq N} \mathbf{h}_i = \frac{1}{N} \sum_{1 \leq i \leq N} h(\mathbf{x}_i)$, and the mean of the c -th class is $\boldsymbol{\mu}^c = \frac{1}{N^c} \sum_{\mathbf{x} \in \mathcal{D}^c} h(\mathbf{x})$.

3.2 Projection Filtering

Pope et al. (2021) demonstrate that high-dimensional image datasets, such as ImageNet, lie in low-dimensional manifolds, despite residing in high-dimensional pixel space. This finding suggests that much of the ambient dimensionality in image data is derived from noise or redundant variation that is not essential to the underlying data-generating process. Motivated by this observation, Principal Component Analysis (PCA) offers a principled way to exploit this low intrinsic dimensionality by filtering out directions in the data that are unlikely to carry meaningful signal, assuming that the true structure of the data is concentrated along a few high-variance directions, whereas noise is distributed more evenly across all dimensions. More specifically, the set of penultimate-layer activations \mathbf{H} are centered by subtracting the mean of each feature: $\bar{\mathbf{H}} = \mathbf{H} - \mathbf{1}_N \boldsymbol{\mu}^\top$. The empirical covariance matrix $\boldsymbol{\Sigma} = \frac{1}{N} \bar{\mathbf{H}}^\top \bar{\mathbf{H}}$ is then decomposed as $\boldsymbol{\Sigma} = \mathbf{V} \boldsymbol{\Lambda} \mathbf{V}^\top$, where \mathbf{V} contains the eigenvectors and $\boldsymbol{\Lambda}$ is the diagonal matrix of eigenvalues $\lambda_1 \geq \lambda_2 \geq \dots \geq \lambda_D$. To denoise the data, only the top k principal components $\mathbf{P} = [\mathbf{v}_1, \dots, \mathbf{v}_k] \in \mathbb{R}^{D \times k}$, which span a subspace that captures most of the variance. The number of components k is decided so that certain percentage of variance is preserved at least. PCA can be applied to both the set of training activa-

tions $\mathbf{H}_{\text{train}}$ centered by the global mean $\boldsymbol{\mu}_{\text{train}}$, from which \mathbf{P} is obtained, and the set of training activations for a given class c , $\mathbf{H}_{\text{train}}^c$, centered by its class mean $\boldsymbol{\mu}_{\text{train}}^c$, from which \mathbf{P}^c is computed.

For a new sample \mathbf{x}_* , the corresponding penultimate-layer activation \mathbf{h}_* is projected onto this subspace: $\mathbf{z}_* = \mathbf{P}^\top(\mathbf{h}_* - \boldsymbol{\mu}) = \mathbf{P}^\top\hat{\mathbf{h}}_* \in \mathbb{R}^k$, and then reconstructed as $\hat{\mathbf{h}}_* = \mathbf{P}\mathbf{z}_* + \boldsymbol{\mu}$. This reconstruction preserves the dominant low-rank structure while discarding low-variance directions. Given that we have global and class subspaces, \mathbf{P} and \mathbf{P}^c respectively, we evaluate multiple projections:

- **Global projection:** $\hat{\mathbf{h}} = \mathbf{P}\mathbf{P}^\top(\mathbf{h} - \boldsymbol{\mu}_{\text{train}}) + \boldsymbol{\mu}_{\text{train}}$
- **Class projection:** $\hat{\mathbf{h}}^c = \mathbf{P}^c\mathbf{P}^{c\top}(\mathbf{h} - \boldsymbol{\mu}_{\text{train}}^c) + \boldsymbol{\mu}_{\text{train}}^c$
- **Class predicted projection:** $\hat{\mathbf{h}}^{\text{pred}} = \hat{\mathbf{h}}^{\hat{y}}$, where $\hat{y} = m(\mathbf{x})$
- **Class projected logit:** $\hat{\mathbf{g}}^{\text{class}} = [\hat{g}^1, \dots, \hat{g}^C]$, where $\hat{g}^c = \mathbf{w}_{cL}^\top \hat{\mathbf{h}}^c + b_{cL}$
- **Global projected probabilities:** $\hat{\mathbf{p}} = \left[\frac{\exp(g(\hat{\mathbf{h}})_1)}{\sum_j \exp(g(\hat{\mathbf{h}})_j)}, \dots, \frac{\exp(g(\hat{\mathbf{h}})_C)}{\sum_j \exp(g(\hat{\mathbf{h}})_j)} \right]$
- **Class projected probabilities:** $\hat{\mathbf{p}}^{\text{class}} = \left[\frac{\exp(\hat{g}^1)}{\sum_j \exp(\hat{g}^j)}, \dots, \frac{\exp(\hat{g}^C)}{\sum_j \exp(\hat{g}^j)} \right]$

All possible OOD detection methods variations that can be derived from these projections are summarized in section A of the Appendix.

3.3 CLIP-based OOD aggregation

We quantify distributional proximity to an arbitrary OOD dataset using the feature space from a CLIP model Radford et al. (2021). Concretely, we extract L2-normalized image embeddings for both ID and candidate OOD sets using a fixed CLIP encoder under identical preprocessing. We then compute two label-agnostic distances between the empirical feature distributions: Fréchet distance (FD) (Dowson and Landau, 1982; Fréchet, 1957) and Maximum Mean Discrepancy (MMD) (Gretton et al., 2006) with a polynomial kernel. Both are evaluated on CLIP embeddings yielding global measures of how close the OOD distribution lies to the ID manifold; by construction, lower values indicate greater proximity.

To capture class-aware proximity, we complement the global measures with two class-conditional dis-

Table 1: OOD dataset clustering. For each source dataset, the corresponding OOD datasets are categorized in near, mid and far datasets based on the CLIP-derived distances.

Source	Near	Mid	Far
CIFAR-10	CIFAR-100, TinyImagenet	iSUN, LSUN(r), LSUN(c), SVHN	Places365, Textures
SuperCIFAR-100	CIFAR-10, TinyImagenet	iSUN, LSUN(r), LSUN(c), SVHN	Places365, Textures
CIFAR-100	CIFAR-10, TinyImagenet	iSUN, LSUN(r), LSUN(c), SVHN	Places365, Textures
Tiny-Imagenet	CIFAR-10, CIFAR-100, iSUN, LSUN(r), LSUN(c)	Places365, Textures	SVHN

tances. First, we represent each ID class by an image-embedding centroid and score a sample by its nearest-centroid angular distance in CLIP feature space. Second, we form text prototypes via prompt ensembling for each ID class (e.g., a photo of a class), embed them with the CLIP text model, and use the maximum image-text cosine similarity. For both class-conditional distances we compute the mean value to quantify a single metric that represents distance to the ID manifold.

All four metrics are oriented so lower implies closer. Finally, we cluster these measurements using KMeans to derive near/mid/far proximity buckets. This protocol is model-agnostic with respect to the downstream OOD detector and applies unchanged to any choice of ID label space. Table 1 shows the resulting clustering and CLIP-derived distances for each dataset are reported in section B of the Appendix.

4 Results

4.1 Experimental Setup

We adopt the FD-Shifts protocol (Jaeger et al., 2022; Traub et al., 2024), which benchmarks CSFs across diverse failure sources and architectures. We consider the following CSF methods: Maximum Softmax Response (MSR) (Hendrycks and Gimpel, 2016), Generalized Entropy (GEN) (Liu et al., 2023) and Renyi Entropy (REN), Predictive Collision Entropy (PCE), GradNorm (Huang et al., 2021), Guessing Entropy (GE), PCA Reconstruction Error (Guan et al., 2023), Class-Typical Matching (CTM) and Class-Typical Matching with mean class features (CTM-mean) (Ngoc-Hieu et al., 2023), Residual and Virtual Logit Matching (ViM) (Wang et al., 2022), Maximum Logit Score (MLS) (Hendrycks et al., 2019), Nearest

Neighbor Guidance (NNGuide) (Park et al., 2023), Neural Collapse-based OOD detection (NeCo) (Ammar et al., 2023), Energy (Liu et al., 2020), Kernel PCA Reconstruction Error (Fang et al., 2025), fast Decision Boundary Decision (fDBD) (Liu and Qin, 2023), Mahalanobis Distance (Maha) (Lee et al., 2018), predictive Normalized Maximum Likelihood (pNML) (Bibas et al., 2021), Confidence (from Confid-Net (Corbiere et al., 2021), DeVries (DeVries and Taylor, 2018), and Deep Gamblers (Liu et al., 2019) training paradigms). VGG-13 and ViT backbone models are trained from scratch and finetuned, respectively, on CIFAR-10, CIFAR-100, SuperCIFAR-100, and Tiny-Imagenet.

All hyperparameters associated to the OOD detection methods are finetuned such that the AUGRC metric is optimized in the validation set. Temperature scaling is tuned on the validation set and applied to all OOD detection methods that used logits as inputs. For Deep Gamblers, the reward is also selected on the validation set. Monte-Carlo Dropout variants (MCD) of the scores named previously are also evaluated, for which we draw 50 stochastic forward passes at test time.

Results are reported on ID test sets and OOD data sets, which are categorized based on CLIP-derived distances. When evaluating OOD detection, we compare OOD samples against only the correctly classified in-distribution (ID) samples and discard ID mistakes, so that a CSF is not rewarded for flagging ordinary in-distribution errors as if they were OOD. Misclassification detection is evaluated separately on the ID test set by ranking correct vs. incorrect ID predictions, so the results still reflect the classifier’s accuracy.

4.2 Statistical Tests

Since we are evaluating multiple CSFs across the same set of blocks where each block is defined by OOD dataset, training paradigm, source, and metric, yielding paired performances, and raw metric scales such as AUGRC or AURC can differ markedly across datasets, we run the Friedman test which is a nonparametric, blocked alternative that converts each block to ranks, so any monotone re-scaling of a block’s metric does not matter. This makes it ideal for CSF evaluation, where distributions are skewed, heteroscedastic, and not commensurate across blocks. Friedman’s test null hypothesis evaluates if average ranks differ across methods, after removing block effects, without assuming Gaussian residuals. If the null hypothesis is rejected, which means that there are different distribution of ranks, we need to determine which groups of CSFs have statistically indistinguishable performance. To achieve this, pairwise differences between CSFs while controlling multiplicity over all pairs

are need. Among rank-based post-hocs approaches, Conover (with Holm correction) provides sharper pairwise calls under the same nonparametric framework. From those adjusted p-values, we construct an Indifference Graph which connects two methods if they are not significantly different. Applying the Bron–Kerbosch algorithm enumerates all maximal sets of CSFs mutually indistinguishable so that top groups of CSFs are generated rather than a brittle single winner. This clique view is (i) faithful to the inferential decisions, and (ii) naturally handles overlaps (a method can belong to multiple near-optimal sets).

4.3 Top Cliques

Figure 1 depicts Conover-Holm top cliques (at $\alpha = 0.05$) across evaluation regimes, with columns denoting settings (e.g., `cifar10→near`, `cifar100→ID`, `tinyimagenet→far`) and rows corresponding to confidence-scoring functions (CSFs) when VGG-13 is the model backbone. Within each column, connected markers indicate the set of methods that are mutually indistinguishable from the best; larger cliques imply broader statistical ties, whereas smaller cliques indicate sharper separation. Shaded bands highlight persistent coalitions that reappear as winners across multiple regimes. In the *source→test* (ID) regime, which corresponds to misclassification detection, probability-based CSFs such as GEN and MSR dominate: here the softmax geometry aligns well with error, so correctly classified ID examples exhibit large logit margins and low predictive entropy, allowing simple confidence/energy scores to rank errors effectively without class-conditional structure.

Across *near* shifts, ENERGY, MLS, and NNGUIDE (especially the global variant) consistently appear in the top cliques. As the semantic distance from the source increases and the number of classes grows (e.g., `cifar100`, `tinyimagenet`), these confidence-style scores become less dominant; geometry-aware CSFs such as fDBD and CTM increasingly anchor the winning sets, reflecting the greater value of boundary proximity and class-typicality under stronger shifts. Notably, CTM is repeatedly selected for `tinyimagenet` (200 classes), consistent with prototype-style scoring benefiting from richer class granularity, while NNGUIDE (global) is among the most frequently retained variants overall, indicating that aggregating neighborhood evidence globally improves OOD discrimination. Finally, as class count rises and shift strength increases from *test→far*, clique sizes tend to contract, underscoring that detector performance depends sensitively on source-label cardinality and shift severity, with fewer methods remaining statistically tied at the top in the harder regimes.

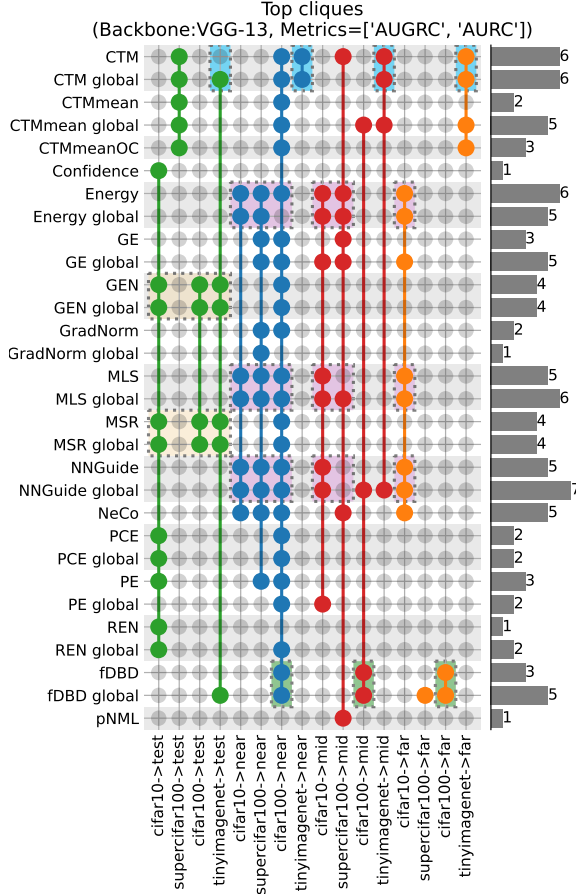


Figure 1: Top-clique map (VGG-13 and AURC/AUGRC metrics): rows are CSF; columns are evaluation regimes labeled “source→test, near, mid, far”. Within each column, connected dots indicate the Conover–Holm top clique ($\alpha=0.05$). Shaded bands emphasize methods that repeatedly appear in top cliques across regimes: probabilistic-derived CSF dominate ID regime, while prototype/geometry-aware methods (CTM-family, NNGuide, fDBD) dominate mid/far. Larger cliques imply many methods are statistically tied at the top; smaller cliques indicate sharper separation.

Figure 2 reports Conover-Holm top cliques at $\alpha = 0.05$ for a ViT backbone. Consistent with the analysis for top cliques when the backbone is VGG-13, in the *source→test* (misclassification) regime, the best-performing confidence-scoring functions (CSFs) are predominantly probabilistic: GEN, MSR, PCE, and REN appear in the top cliques across class counts. In contrast to the CNN case, CTM contributes less in the *mid* and *far* regimes. A plausible explanation is that CTM relies on class feature prototypes whose utility can diminish after fine-tuning a large, pretrained ViT. Fine-tuning sharpens decision boundaries for the *source* task while partially reshaping prototype geom-

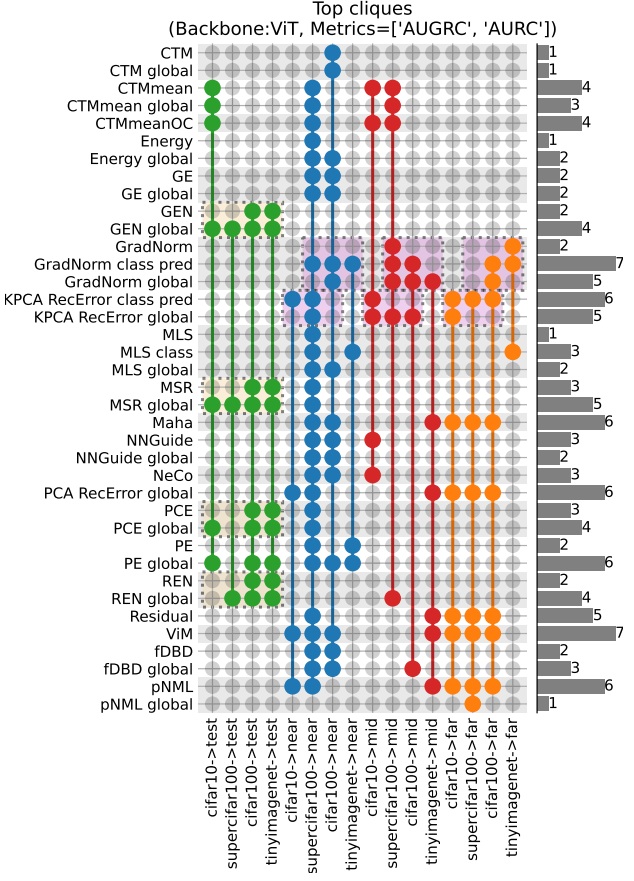


Figure 2: Top cliques for ViT (AUGRC/AURC). Columns are source→test, near, mid, far; rows are methods. Connected dots indicate the Conover–Holm top clique in each column; shaded bands mark coalitions that recur across regimes. ViT exhibits persistent top groups centered on GradNorm and KPCA RecError. Similar to the VGG-13 results. Misclassification regime sis dominated by probabilistic-derived CSFs.

etry, reducing CTM’s discriminative advantage under stronger shifts. Two methods that remain consistently competitive are GRADNORM and KPCA RECERROR; in our results, GRADNORM improves as the number of classes grows (larger label spaces yield tighter, more curved decision regions where gradient-based margin proxies are informative), whereas KPCA is comparatively stronger at smaller class counts (lower intrinsic dimensionality makes reconstruction error more stable).

Across *near*, *mid*, and *far* shifts, the *near* columns retain the largest cliques, while *mid* and *far* typically admit fewer top-tied CSFs. This mirrors the observation that, under fine-tuning, *mid* and *far* shifts present similar difficulty. Pretraining exposes ViT to semantically related categories, and fine-tuning adjusts boundaries

to the source classes while preserving partial structure from pretraining, limiting the number of clearly superior CSFs as shift severity increases. Notably, using the *class-pred* projection, which is the subspace selected by the predicted class, boosts KPCA RECER-ROR, but specially GRADNORM, likely because this projection leverages the classifier’s own discrimination to choose a feature subspace where margin curvature better separate atypical examples. Finally, ViM shows a strong presence in *near* and *far* but not *mid*, consistent with its reliance on virtual-logit structure that is effective when the shift is either small (logit geometry remains reliable) or very large (clear separation), but less decisive in intermediate, confusable conditions.

4.4 MCD vs non-MCD performance

Table 2 presents a comprehensive evaluation of various model configurations and training methodologies for selective classification, with performance measured by the Area Under the Generalized Risk-Coverage (AUGRC) curve. Only the best performing scores for each source and ID/OOD datasets are shown.

The most prominent finding is the trade-off between standard inference and Monte Carlo Dropout (MCD) as a function of the number of classes. For datasets with a low number of classes (e.g., 10 classes), models evaluated without MCD consistently achieve lower AUGRC scores. This suggests that for simpler tasks, methods that directly learn a confidence score, like those from the Deep Gamblers (DG) framework, are more effective at providing a reliable uncertainty estimate. However, as the number of classes increases, the performance of models evaluated with MCD improves significantly and often surpasses that of non-MCD methods. This indicates that for complex classification tasks, the epistemic uncertainty captured by MC dropout provides a more robust signal for selective classification.

The choice of training method is also critical for optimizing performance, with different approaches yielding the best results depending on the intended inference strategy. When using MCD for inference, models trained with ConfidNet produce the best AUGRC scores across the board. When MCD is not an option at inference time, the Deep Gamblers dg training method stands out. This end-to-end approach reframes selective classification as a gambling problem, learning to “abstain” from making a prediction when the confidence is low. Our results show that this method produces the best AUGRC scores for non-MCD scenarios, regardless of whether dropout layers were used during training.

Table 2: Best IID (rows labeled test) and OOD (other rows) AUGRC scores and model configurations. This table summarizes the performance of various selective classification models, with results evaluated using the AUGRC metric. The findings demonstrate a clear dependence on dataset complexity. For datasets with a low number of classes, non-MCD methods, particularly the Deep Gamblers (DG) model, achieve superior AUGRC scores. Conversely, as the number of classes increases, Monte Carlo Dropout (MCD) with models trained using the **confidnet** method becomes the optimal approach.

		nonMCD AUGRC	MCD AUGRC	nonMCD paradigm	MCD paradigm
cifar10	test	3.9132	4.5384	DG	confidnet
	cifar100	163.4954	163.3573	confidnet	confidnet
	tinyimagenet	149.7686	150.2396	confidnet	confidnet
	isun	133.5868	133.8892	confidnet	confidnet
	lsun	148.6756	150.3665	DG	confidnet
	cropped				
	lsun resize	148.4497	148.7788	confidnet	confidnet
	places365	159.3993	161.7047	DG	confidnet
	textures	88.0191	89.9795	DG	DeVries
supercifar100	svhn	287.3275	287.7814	DG	DeVries
	test	145.7328	144.6418	DG	DG
	cifar10	266.3995	267.6652	confidnet	DG
	tinyimagenet	232.1150	225.5546	DG	DG
	isun	221.0056	215.9046	DG	DG
	lsun	229.9232	234.8684	DG	confidnet
	cropped				
	lsun resize	237.1198	230.2041	DG	DG
	textures	158.8078	162.8347	DG	confidnet
cifar100	places365	264.2114	263.4520	DG	confidnet
	svhn	346.4916	354.0474	DG	confidnet
	test	54.3580	52.6486	DeVries	DG
	cifar10	209.7024	209.9227	DeVries	DG
	tinyimagenet	195.6496	195.5451	confidnet	confidnet
	isun	181.3098	185.1370	DeVries	confidnet
	lsun	196.5520	194.7769	DG	confidnet
	cropped				
	lsun resize	196.2106	197.8931	DG	confidnet
tinyimagenet	textures	125.4978	121.1945	DeVries	confidnet
	places365	210.3229	211.2779	DeVries	confidnet
	svhn	326.7164	322.6135	DG	confidnet
	test	97.0525	91.3660	DG	DG
	cifar100	219.9844	215.7338	confidnet	confidnet
	cifar10	214.7156	209.2819	confidnet	confidnet
	isun	195.8857	189.4729	DG	confidnet
	places365	223.5343	218.2668	DG	DeVries
	lsun resize	211.7826	205.5667	DG	confidnet
	textures	150.5724	146.8387	confidnet	confidnet
	lsun	209.3178	205.0045	DG	confidnet
	cropped				
	svhn	344.5073	340.2405	DG	DeVries

4.4.1 Limitations

Our study focuses on image classification with a restricted set of sources and shifts (CIFAR-10/100, super-CIFAR-100, TinyImageNet, and common near/mid/far OOD benchmarks), two backbone regimes (a scratch-trained CNN and a fine-tuned ViT), and a curated portfolio of confidence-scoring functions (CSFs). While this choice enables careful, paired comparisons and rigorous statistics, it limits external validity: results may not transfer to larger or newer backbones, self-supervised foundations, multi-label settings, detection/segmentation, or

distribution drifts that are temporal, causal, or task-specific. Our CLIP-based grouping uses a fixed encoder and k -means with $k = 3$; both the encoder and clustering hyperparameters can influence the notion of “semantic distance.” Metric coverage is also incomplete: we emphasize threshold-free ranking metrics AURC/AUGRC, but do not fully explore cost-sensitive operating points, deployment-specific utility, or calibration–utility trade-offs under label shift. Finally, the ViT is fine-tuned from a large pretrained model; potential latent overlap with OOD categories was not exhaustively audited and could advantage prototype-style scoring in subtle ways.

Our rank-based pipeline (Friedman → Conover with Holm correction → Bron–Kerbosch cliques) provides robust, multiple-comparison-controlled summaries, but inherits assumptions of complete blocks and exchangeability; effect sizes are not directly encoded in clique membership, and different post-hoc choices (e.g., Nemenyi, Quade, SC all-pairs) can yield slightly different borders for “indistinguishable” sets. Hyperparameter sweeps (e.g., DG rewards, kernel bandwidths for KPCA, temperature scaling, etc) were optimized on the validation set to achieve the best AUGRC, and the best performing CSFs might change if another metric is used. Also, we did not evaluate computational cost or latency—factors that matter in deployment and may re-rank methods under real-time constraints.

4.5 Computing Infrastructure

All experiments were executed on our internal GPU cluster. *CNN* runs (VGG-13 trained from scratch) were scheduled on NVIDIA T4 GPUs, while *ViT* runs (fine-tuned from a large pretrained model) were scheduled on NVIDIA A100 GPUs. We did not mix GPU types within an experiment. Every training/evaluation job for a given backbone used the same GPU class to avoid hardware-induced variance.

4.6 Conclusion

Our study provides evidence that OOD detection performance is primarily governed by the structure of the learned representation rather than the sophistication of the scoring rule. Across CLIP-stratified regimes (ID/near/mid/far) and two backbone paradigms (scratch-trained VGG-13 compared to fine-tuned ViT), rank-based meta-analysis (Friedman → Conover–Holm) with Bron–Kerbosch cliques shows:

1. On CNNs, ranking quality is margin-driven on ID/near (Energy/MLS/MSR), while geometry-aware scores (NNGuide, fDBD, CTM) dominate

mid/far.

2. On ViTs, probabilistic scores (GEN/MSR/REN/PCE) remain competitive across regimes, with GradNorm/KPCA RecError contributing when class granularity changes.
3. Monte-Carlo Dropout yields a class-count-dependent trade-off (beneficial as the label space grows, less so on simple tasks).
4. PCA projection improves several methods by filtering directions that do not support class-consistent structure.

Practically, our results argue for representation-aware selection: prefer margin/energy on ID/near, add prototype/neighbor/boundary cues as shift grows, and consider MCD when the class space is large. Limitations include the image-classification focus, unequal dataset sizes, and constrained hyperparameter grids; we encourage future work on self-supervised backbones, temporal drift, and cost-sensitive operating points.

References

Ammar, M. B., Belkhir, N., Popescu, S., Manzanera, A., and Franchi, G. (2023). Neco: Neural collapse based out-of-distribution detection. *arXiv preprint arXiv:2310.06823*.

Bibas, K., Feder, M., and Hassner, T. (2021). Single layer predictive normalized maximum likelihood for out-of-distribution detection. *Advances in Neural Information Processing Systems*, 34:1179–1191.

Bron, C. and Kerbosch, J. (1973). Algorithm 457: finding all cliques of an undirected graph. *Communications of the ACM*, 16(9):575–577.

Bungert, T. J., Kobelke, L., and Jaeger, P. F. (2023). Understanding silent failures in medical image classification. In *International conference on medical image computing and computer-assisted intervention*, pages 400–410. Springer.

Conover, W. J. (1999). *Practical nonparametric statistics*. John Wiley & Sons.

Corbière, C., Thome, N., Bar-Hen, A., Cord, M., and Pérez, P. (2019). Addressing failure prediction by learning model confidence. *Advances in neural information processing systems*, 32.

Corbière, C., Thome, N., Saporta, A., Vu, T.-H., Cord, M., and Pérez, P. (2021). Confidence estimation via auxiliary models. *IEEE Transactions on Pattern Analysis and Machine Intelligence*, 44(10):6043–6055.

Cover, T. M. and Thomas, J. A. (2006). *Elements of Information Theory (Wiley Series in Telecommunications and Signal Processing)*. Wiley-Interscience, USA.

Demšar, J. (2006). Statistical comparisons of classifiers over multiple data sets. *Journal of Machine learning research*, 7(Jan):1–30.

Deng, J., Dong, W., Socher, R., Li, L.-J., Li, K., and Fei-Fei, L. (2009). Imagenet: A large-scale hierarchical image database. In *2009 IEEE conference on computer vision and pattern recognition*, pages 248–255. Ieee.

DeVries, T. and Taylor, G. W. (2018). Learning confidence for out-of-distribution detection in neural networks. *arXiv preprint arXiv:1802.04865*.

Dowson, D. and Landau, B. (1982). The fréchet distance between multivariate normal distributions. *Journal of multivariate analysis*, 12(3):450–455.

Fang, K., Tao, Q., He, M., Lv, K., Yang, R., Hu, H., Huang, X., Yang, J., and Cao, L. (2025). Kernel pca for out-of-distribution detection: Non-linear kernel selections and approximations. *arXiv preprint arXiv:2505.15284*.

Fréchet, M. (1957). Sur la distance de deux lois de probabilité. In *Annales de l'ISUP*, volume 6, pages 183–198.

Gal, Y. and Ghahramani, Z. (2016). Dropout as a bayesian approximation: Representing model uncertainty in deep learning. In *international conference on machine learning*, pages 1050–1059. PMLR.

Geifman, Y., Uziel, G., and El-Yaniv, R. (2018). Bias-reduced uncertainty estimation for deep neural classifiers. *arXiv preprint arXiv:1805.08206*.

Granese, F., Romanelli, M., Gorla, D., Palamidessi, C., and Piantanida, P. (2021). Doctor: A simple method for detecting misclassification errors. *Advances in Neural Information Processing Systems*, 34:5669–5681.

Gretton, A., Borgwardt, K., Rasch, M., Schölkopf, B., and Smola, A. (2006). A kernel method for the two-sample-problem. *Advances in neural information processing systems*, 19.

Guan, X., Liu, Z., Zheng, W.-S., Zhou, Y., and Wang, R. (2023). Revisit pca-based technique for out-of-distribution detection. In *Proceedings of the IEEE/CVF international conference on computer vision*, pages 19431–19439.

Gutbrod, M., Rauber, D., Nunes, D. W., and Palm, C. (2025). Openmibood: Open medical imaging benchmarks for out-of-distribution detection. *arXiv preprint arXiv:2503.16247*.

Hendrycks, D., Basart, S., Mazeika, M., Zou, A., Kwon, J., Mostajabi, M., Steinhardt, J., and Song, D. (2019). Scaling out-of-distribution detection for real-world settings. *arXiv preprint arXiv:1911.11132*.

Hendrycks, D. and Gimpel, K. (2016). A baseline for detecting misclassified and out-of-distribution examples in neural networks. *arXiv preprint arXiv:1610.02136*.

Holm, S. (1979). A simple sequentially rejective multiple test procedure. *Scandinavian journal of statistics*, pages 65–70.

Huang, R., Geng, A., and Li, Y. (2021). On the importance of gradients for detecting distributional shifts in the wild. *Advances in Neural Information Processing Systems*, 34:677–689.

Iman, R. L. and Davenport, J. M. (1980). Approximations of the critical region of the fbietkan statistic. *Communications in Statistics-Theory and Methods*, 9(6):571–595.

Jaeger, P. F., Lüth, C. T., Klein, L., and Bungert, T. J. (2022). A call to reflect on evaluation practices for failure detection in image classification. *arXiv preprint arXiv:2211.15259*.

Lee, K., Lee, K., Lee, H., and Shin, J. (2018). A simple unified framework for detecting out-of-distribution samples and adversarial attacks. *Advances in neural information processing systems*, 31.

Liu, L. and Qin, Y. (2023). Fast decision boundary based out-of-distribution detector. *arXiv preprint arXiv:2312.11536*.

Liu, W., Wang, X., Owens, J., and Li, Y. (2020). Energy-based out-of-distribution detection. *Advances in neural information processing systems*, 33:21464–21475.

Liu, X., Lochman, Y., and Zach, C. (2023). Gen: Pushing the limits of softmax-based out-of-distribution detection. In *Proceedings of the IEEE/CVF conference on computer vision and pattern recognition*, pages 23946–23955.

Liu, Z., Wang, Z., Liang, P. P., Salakhutdinov, R. R., Morency, L.-P., and Ueda, M. (2019). Deep gamblers: Learning to abstain with portfolio theory. *Advances in Neural Information Processing Systems*, 32.

Massey, J. L. (1994). Guessing and entropy. In *Proceedings of 1994 IEEE International Symposium on Information Theory*, page 204. IEEE.

Ngoc-Hieu, N., Hung-Quang, N., Ta, T.-A., Nguyen-Tang, T., Doan, K. D., and Thanh-Tung, H. (2023). A cosine similarity-based method

for out-of-distribution detection. *arXiv preprint arXiv:2306.14920*.

Ovadia, Y., Fertig, E., Ren, J., Nado, Z., Sculley, D., Nowozin, S., Dillon, J., Lakshminarayanan, B., and Snoek, J. (2019). Can you trust your model’s uncertainty? evaluating predictive uncertainty under dataset shift. *Advances in neural information processing systems*, 32.

Papyan, V., Han, X., and Donoho, D. L. (2020). Prevalence of neural collapse during the terminal phase of deep learning training. *Proceedings of the National Academy of Sciences*, 117(40):24652–24663.

Park, J., Jung, Y. G., and Teoh, A. B. J. (2023). Nearest neighbor guidance for out-of-distribution detection. In *Proceedings of the IEEE/CVF international conference on computer vision*, pages 1686–1695.

Pope, P., Zhu, C., Abdelkader, A., Goldblum, M., and Goldstein, T. (2021). The intrinsic dimension of images and its impact on learning. *arXiv preprint arXiv:2104.08894*.

Radford, A., Kim, J. W., Hallacy, C., Ramesh, A., Goh, G., Agarwal, S., Sastry, G., Askell, A., Mishkin, P., Clark, J., et al. (2021). Learning transferable visual models from natural language supervision. In *International conference on machine learning*, pages 8748–8763. PMLR.

Rényi, A. (1961). On measures of entropy and information. In *Proceedings of the fourth Berkeley symposium on mathematical statistics and probability, volume 1: contributions to the theory of statistics*, volume 4, pages 547–562. University of California Press.

Shannon, C. E. (1948). A mathematical theory of communication. *The Bell system technical journal*, 27(3):379–423.

Traub, J., Bungert, T. J., Lüth, C. T., Baumgartner, M., Maier-Hein, K. H., Maier-Hein, L., and Jaeger, P. F. (2024). Overcoming common flaws in the evaluation of selective classification systems. *arXiv preprint arXiv:2407.01032*.

Wang, H., Li, Z., Feng, L., and Zhang, W. (2022). Vim: Out-of-distribution with virtual-logit matching. In *Proceedings of the IEEE/CVF conference on computer vision and pattern recognition*, pages 4921–4930.

Yang, J., Wang, P., Zou, D., Zhou, Z., Ding, K., Peng, W., Wang, H., Chen, G., Li, B., Sun, Y., et al. (2022). Openood: Benchmarking generalized out-of-distribution detection. *Advances in Neural Information Processing Systems*, 35:32598–32611.

Zhang, J., Yang, J., Wang, P., Wang, H., Lin, Y., Zhang, H., Sun, Y., Du, X., Li, Y., Liu, Z., et al. (2023). Openood v1.5: Enhanced benchmark for out-of-distribution detection. *arXiv preprint arXiv:2306.09301*.

Checklist

1. For all models and algorithms presented, check if you include:
 - (a) A clear description of the mathematical setting, assumptions, algorithm, and/or model. [Yes]
 - (b) An analysis of the properties and complexity (time, space, sample size) of any algorithm. [Not Applicable]
 - (c) (Optional) Anonymized source code, with specification of all dependencies, including external libraries. [Yes]
2. For any theoretical claim, check if you include:
 - (a) Statements of the full set of assumptions of all theoretical results. [Not Applicable]
 - (b) Complete proofs of all theoretical results. [Not Applicable]
 - (c) Clear explanations of any assumptions. [Not Applicable]
3. For all figures and tables that present empirical results, check if you include:
 - (a) The code, data, and instructions needed to reproduce the main experimental results (either in the supplemental material or as a URL). [Yes]
 - (b) All the training details (e.g., data splits, hyperparameters, how they were chosen). [Yes]
 - (c) A clear definition of the specific measure or statistics and error bars (e.g., with respect to the random seed after running experiments multiple times). [Yes]
 - (d) A description of the computing infrastructure used. (e.g., type of GPUs, internal cluster, or cloud provider). [Yes]
4. If you are using existing assets (e.g., code, data, models) or curating/releasing new assets, check if you include:
 - (a) Citations of the creator If your work uses existing assets. [Yes]
 - (b) The license information of the assets, if applicable. [Not Applicable]
 - (c) New assets either in the supplemental material or as a URL, if applicable. [Not Applicable]

- (d) Information about consent from data providers/curators. [Not Applicable]
- (e) Discussion of sensible content if applicable, e.g., personally identifiable information or offensive content. [Not Applicable]

5. If you used crowdsourcing or conducted research with human subjects, check if you include:

- (a) The full text of instructions given to participants and screenshots. [Not Applicable]
- (b) Descriptions of potential participant risks, with links to Institutional Review Board (IRB) approvals if applicable. [Not Applicable]
- (c) The estimated hourly wage paid to participants and the total amount spent on participant compensation. [Not Applicable]

A Systematic Analysis of Out-of-Distribution Detection Under Representation and Training Paradigm Shifts: Supplementary Materials

A Training Paradigms, CFS Baselines and Variations

A.1 Training Paradigms

A.1.1 ConfidNet (regressing the true-class probability).

Let $f_{\mathcal{W}} = g \circ h$ be a trained classifier with weights \mathcal{W} , logits $f(\mathbf{x}) \in \mathbb{R}^K$ and softmax $p_k(\mathbf{x}) = \exp(f_k(\mathbf{x}))/\sum_j \exp(f_j(\mathbf{x}))$. The standard confidence proxy is the maximum class probability, $\text{MSR}(\mathbf{x}) = \max_{k \in \{1, \dots, K\}} p_k(\mathbf{x})$, but this quantity can be spuriously large for both correct and erroneous predictions, hampering failure detection. ConfidNet replaces MSR with the *true-class probability* (TCP), $\text{TCP}(\mathbf{x}, y) = p_y(\mathbf{x})$, which is typically high for correct predictions and low for misclassifications (Corbière et al., 2019; Corbière et al., 2021). Because y is unknown at test time, ConfidNet learns an auxiliary regressor $s_{\mathcal{W}^{\text{conf}}} : \mathcal{X} \rightarrow [0, 1]$ that *predicts* $\text{TCP}(\mathbf{x}, y)$ from features of the trained classifier $f_{\mathcal{W}}$.

Denote by $E = h$ the encoder of $f_{\mathcal{W}}$ and by $g_{\mathcal{W}^{\text{conf}}} : \mathbb{R}^D \rightarrow [0, 1]$ a small MLP head. ConfidNet’s score is $s_{\mathcal{W}^{\text{conf}}}(\mathbf{x}) = (g_{\mathcal{W}^{\text{conf}}} \circ E)(\mathbf{x}) \approx \text{TCP}(\mathbf{x}, y)$, trained on the labeled training set $\mathcal{D}_{\text{train}}$ with a mean squared error loss $\mathcal{L}_{\text{conf}}(\mathcal{W}^{\text{conf}}; \mathcal{D}_{\text{train}}) = \frac{1}{|\mathcal{D}_{\text{train}}|} \sum_{(\mathbf{x}_i, y_i) \in \mathcal{D}_{\text{train}}} (s_{\mathcal{W}^{\text{conf}}}(\mathbf{x}_i) - \text{TCP}(\mathbf{x}_i, y_i))^2$. This *post-hoc* module transfers knowledge from the classifier’s encoder and yields a calibrated, label-informed confidence score at inference. It should be noted that the weights \mathcal{W} are kept frozen when training $g_{\mathcal{W}^{\text{conf}}}$. In practice, ConfidNet can be viewed as a supervised alternative to MSR that aligns the confidence target with the Bayes-relevant quantity TCP; see Corbière et al. (2019); Corbière et al. (2021) for more details on the implementation.

A.1.2 DeVries & Taylor: learned confidences via target–prediction interpolation.

Given a classifier $f_{\mathcal{W}} = g \circ h$ with softmax $p(\mathbf{x}) \in \Delta^{K-1}$, DeVries and Taylor (2018) add a *confidence branch* in parallel to the class head. The branch shares features with the penultimate layer and outputs $s_{\mathcal{W}^{\text{devries}}}(\mathbf{x}) = \sigma(\mathbf{w}^\top h(\mathbf{x}) + b) \in [0, 1]$, interpreted as the network’s confidence that it can correctly predict the label of \mathbf{x} . During training, the method provides the network with “hints” by *interpolating* between its own prediction and the one-hot target \mathbf{y} according to s : $s'(\mathbf{x}, \mathbf{y}) = s_{\mathcal{W}^{\text{devries}}}(\mathbf{x}) p(\mathbf{x}) + (1 - s_{\mathcal{W}^{\text{devries}}}(\mathbf{x})) \mathbf{y}$. The task loss is then computed on s' rather than on p , e.g. the negative log-likelihood $\mathcal{L}_{\text{task}}(\mathcal{W}^{\text{devries}}, \mathcal{W}) = -\frac{1}{|\mathcal{D}_{\text{train}}|} \sum_{(\mathbf{x}_i, y_i)} \log([p'(\mathbf{x}_i, y_i)]_{y_i})$. Intuitively, when the model is *uncertain* ($s \approx 0$), it is allowed to rely more on the target distribution (a hint); when it is *confident* ($s \approx 1$), it must stand by its own prediction.

To avoid the degenerate solution $s = 0$ (which would always copy the target), a confidence regularizer encourages high s values: $\mathcal{L}_{\text{devries}}(\mathcal{W}^{\text{devries}}) = -\frac{1}{|\mathcal{D}_{\text{train}}|} \sum_{\mathbf{x}_i} \log s_{\mathcal{W}^{\text{conf}}}(\mathbf{x}_i)$, $\mathcal{L}_{\text{total}} = \mathcal{L}_{\text{task}} + \lambda \mathcal{L}_{\text{devries}}$, with $\lambda > 0$ balancing reliance on hints versus self-prediction. The resulting balancing where copying the target when the classifier struggles vs. being penalized for low confidence drives $s(\mathbf{x})$ to be large where the model is accurate and small where it is prone to error. At test time, the class prediction uses $p(\mathbf{x})$ from the base head, while $s(\mathbf{x})$ serves as a *confidence score* for failure/OOD detection; no hints are used at inference. See DeVries and Taylor (2018) for more details on the implementation.

A.1.3 Deep Gamblers: abstention via a $(K+1)$ -st class and a reward parameter.

Liu et al. (2019) cast classification as a Kelly-style gambling game (Cover and Thomas, 2006). For a K -class task, the network predicts over $K+1$ outcomes. This means that an additional *abstain* option is attached to the original K labels. Let $f_{\mathcal{W}} = g \circ h$ with logits $f(\mathbf{x}) \in \mathbb{R}^{K+1}$, $p(\mathbf{x}) = \text{softmax}(f(\mathbf{x})) \in \Delta^K$, and write $p_k(\mathbf{x})$ for

class $k \leq K$ and $p_{K+1}(\mathbf{x})$ for *abstain*. The training objective maximizes the expected (log) wealth in a horse-race with *reservation*: predicting the true class y yields payoff $o > 0$ (a tunable *reward*), and abstaining yields payoff 1. This leads to the loss $\mathcal{L}_{\text{DG}}(\mathcal{W}; \mathcal{D}_{\text{train}}, o) := -\frac{1}{|\mathcal{D}_{\text{train}}|} \sum_{(\mathbf{x}_i, y_i) \in \mathcal{D}_{\text{train}}} \log(o p_{y_i}(\mathbf{x}_i) + p_{K+1}(\mathbf{x}_i))$.

When $p_{K+1} = 0$ (no abstention), \mathcal{L}_{DG} reduces to cross-entropy up to an additive constant (since $\log o$ adds to the true-class logit). The head is linear, $g(z) = Wz + b$, $W \in \mathbb{R}^{(K+1) \times D}$, $b \in \mathbb{R}^{K+1}$, so the method is a drop-in replacement for a standard classifier.

At test time, the model accepts an output if its (reward-weighted) probability dominates abstention, and rejects otherwise. A sufficient decision rule is $\text{accept} \Leftrightarrow o \cdot \max_{k \leq K} p_k(\mathbf{x}) > p_{K+1}(\mathbf{x})$, reject (abstain) otherwise. Hence, larger o discourages abstention (the classifier must be more confident to reject), while smaller o encourages it. o is tuned on validation to meet a desired risk-coverage trade-off. For failure/OOD detection one can use the abstention mass as a score, $s_{\text{DG}}(\mathbf{x}) = p_{K+1}(\mathbf{x})$ (higher \Rightarrow more likely atypical), or a margin-like variant $s_{\text{DG}}(\mathbf{x}) = p_{K+1}(\mathbf{x}) - o \cdot \max_{k \leq K} p_k(\mathbf{x})$ (negative \Rightarrow accept). The former is used in this work. The $(K+1)$ -st class thus implements a principled, calibrated abstention mechanism consistent with the Kelly criterion, while keeping the architecture and training pipeline simple. See [Liu et al. \(2019\)](#) for details on the implementation and effect of o .

Note

Unlike DeVries & Taylor ([DeVries and Taylor, 2018](#)) and Deep Gamblers ([Liu et al., 2019](#)), ConfidNet ([Corbière et al., 2019; Corbiere et al., 2021](#)) fine-tunes a copy of a trained encoder h to generate the confidence score $s_{\mathcal{W}^{\text{conf}}}$. This copy does not modify f which is the output used to train and evaluate the ID/OOD detection methods. In fact, f in the ConfidNet training paradigm is the result of a *conventional* training approach, which is guided by the minimization of the cross-entropy loss.

A.2 ID/OOD Detection Methods

This section describes all the CSFs and their variations after applying the Projection Filtering described in section [3.2](#).

A.2.1 Class Typical Matching (CTM) and Class Typical Matching with class means prototypes (CTMmean) ([Ngoc-Hieu et al., 2023](#))

Prototype matching in feature space consists of quantifying the similarity between a sample \mathbf{x} and the last-layer trained weights $\{\mathbf{w}_1, \dots, \mathbf{w}_K\}$. Therefore the similarity to the closest trained weight is $\text{CTM}(\mathbf{x}) = \max_{k \leq C} \text{sim}(\mathbf{w}_k, \mathbf{h})$. Alternatively, we can compute class means $\boldsymbol{\mu}_{\text{train}}^c$ and score by similarity to the closest class mean, $\text{CTMmean}(\mathbf{x}) = \max_{k \leq C} \text{sim}(\boldsymbol{\mu}_{\text{train}}^k, \mathbf{h})$. Following [Ngoc-Hieu et al. \(2023\)](#), we use cosine similarity in this work, where $\text{sim}(\mathbf{u}, \mathbf{v}) = \frac{\mathbf{u}^\top \mathbf{v}}{\|\mathbf{u}\|_2 \|\mathbf{v}\|_2}$. CTM scores the *typicality* of \mathbf{x} by comparing its feature \mathbf{h} against a bank of class representatives. Higher similarity indicates greater in-distribution (ID) conformity.

A.2.2 Energy ([Liu et al., 2020](#))

The energy score is defined as $\text{Energy}(\mathbf{x}) = -T \log \sum_{k=1}^C \exp(g(\mathbf{h})_k/T)$, with temperature $T > 0$. Higher Energy score typically indicates higher uncertainty.

A.2.3 Maximum Softmax Response (MSR) ([Hendrycks and Gimpel, 2016](#)) and Maximum Logit Score (MLS) ([Hendrycks et al., 2019](#))

A baseline confidence score given by the maximum predicted probability $\text{MSR}(\mathbf{x}) = \max_{k \leq C} p_k$, widely used for OOD detection. Lower values indicate atypical inputs. Similarly, MLS is a confidence score measured in the logit space, $\text{MLS}(\mathbf{x}) = \max_{k \leq C} g(\mathbf{h})_k$, often more stable than softmax under temperature changes.

A.2.4 Predictive Entropy (PE), Generalized Entropy (GEN), Renyi Entropy (REN), Guessing Entropy (GE), and Predictive Collision Entropy (PCE)

Predictive Entropy (PE) (Ovadia et al., 2019). Uncertainty via Shannon entropy (Shannon, 1948) of the predictive distribution $\text{PE}(\mathbf{x}) = H(p(\mathbf{x})) = -\sum_{k=1}^C \mathbf{p}_k \log \mathbf{p}_k$, with larger entropy signaling higher uncertainty.

Generalized Entropy (GEN) (Liu et al., 2023). GEN is a post-hoc OOD score that uses the softmax probabilities of a trained classifier. Let $\mathbf{p}_{(1)} \geq \dots \geq \mathbf{p}_{(K)}$ denote the probabilities sorted in descending order for a given input \mathbf{x} . For sensitivity and numerical stability in many-class settings, GEN truncates to the top- M classes and computes a generalized entropy with exponent $\gamma \in (0, 1)$: $\text{GEN}(\mathbf{x}) = \sum_{k=1}^M \mathbf{p}_{(k)}^\gamma (1 - \mathbf{p}_{(k)})^\gamma$. The confidence score is the *negated* generalized entropy so that a larger GEN (lower entropy) indicates more ID-like predictions.

Rényi Entropy (REN). The Rényi entropy (Rényi, 1961) of order α is a smooth generalization of Shannon entropy that emphasizes different parts of the distribution. Similar to GEN, REN is defined by a truncation parameter M and exponent $\alpha \in (0, 1)$: $\text{REN}(\mathbf{x}) = \frac{1}{1-\alpha} \log \sum_{k=1}^M \mathbf{p}_{(k)}^\alpha$.

Guessing Entropy (GE). GE (Massey, 1994) quantifies the expected number of guesses to identify the true class when labels are guessed in decreasing probability $p_k(\mathbf{x})$: if $p_{(1)} \geq \dots \geq p_{(K)}$ are sorted, then $\text{GE}(\mathbf{x}) = \sum_{k=1}^C k \mathbf{p}_{(k)}$, with larger values denoting higher uncertainty.

Predictive Collision Entropy (PCE) (Granese et al., 2021). PCE measures prediction uncertainty via the *collision* (order-2 Rényi) entropy of the softmax distribution: $\text{PCE}(\mathbf{x}) = -\log \sum_{k=1}^C \mathbf{p}_k^2$. Since $\sum_k \mathbf{p}_k^2$ is the “collision probability,” PCE grows as the distribution spreads (uncertain/atypical) and shrinks as it peaks (confident/ID-like). This uncertainty score uses the entire predictive distribution rather than just its maximum.

A.2.5 Mahalanobis Distance (Maha) (Lee et al., 2018)

Assuming Gaussian class-conditional features, score by the (negative) Mahalanobis distance to the nearest class centroid is $\text{Maha}(\mathbf{x}) = \max_{k \leq C} (\mathbf{h}(\mathbf{x}) - \boldsymbol{\mu}_{\text{train}}^k)^\top \boldsymbol{\Sigma}^{-1} (\mathbf{h}(\mathbf{x}) - \boldsymbol{\mu}_{\text{train}}^k) = \bar{\mathbf{h}}_k^\top \boldsymbol{\Sigma}^{-1} \bar{\mathbf{h}}_k$, where $\boldsymbol{\Sigma}$ is the empirical covariance matrix.

A.2.6 Nearest Neighbor Guide (NNGuide) (Park et al., 2023)

NNGuide is a post-hoc wrapper that modulates any classifier-based OOD score $S_{\text{base}}(\mathbf{h})$ using nearest neighbors from an ID bank of features. This bank is formed by sampling $\alpha \in (0, 1)$ of ID training features \mathbf{h}_i (L2-normalized) and their base scores $s_i = S_{\text{base}}(\mathbf{h}_i)$. More specifically, given an input \mathbf{x} , the corresponding feature \mathbf{h} (L2-normalized) defines a confidence-scaled similarity list $\{s_i \cos(\mathbf{h}, \mathbf{h}_i)\}_{i=1}^N$, which is sampled by taking the top- k terms, where $k = \lfloor \alpha N \rfloor$. The top- k terms set the guidance $G(\mathbf{h}) = \frac{1}{k} \sum_{i \leq k} s_i \cos(\mathbf{h}, \mathbf{h}_i)$, and the score $\text{NNGuide}(\mathbf{x}) = S_{\text{base}}(\mathbf{h}) \cdot G(\mathbf{h})$. In practice, S_{base} is the (negative) Energy score, but NNGuide can improve other classifier-based scores. Intuitively, $G(\mathbf{h})$ down-scales overconfident far-OOD points where cosine similarities are small and preserves near-ID points using high-confidence neighbors.

A.2.7 fast Decision Boundary Detector (fDBD) (Liu and Qin, 2023)

fDBD scores a sample by how far its feature lies from the nearest class decision boundary, regularized by feature deviation from the in-distribution mean. For each non-predicted class $c \neq m(\mathbf{x})$, the (unknown) distance in the feature space to the c -boundary is lower bounded by $D_g(\mathbf{h}, k) = \frac{|(\mathbf{w}_m - \mathbf{w}_k)^\top \mathbf{h} + (b_m - b_k)|}{\|\mathbf{w}_m - \mathbf{w}_k\|_2}$, i.e., the Euclidean distance from \mathbf{h} to the separating hyperplane between classes $m(\mathbf{x})$ and c . Averaging these distances and *regularizing* by the feature’s deviation from the ID mean $\boldsymbol{\mu}_{\text{train}}$ yields the score $\text{fDBD}(\mathbf{x}) = \frac{1}{C-1} \sum_{k=1}^C \sum_{k \neq m(\mathbf{x})} \frac{D_g(\mathbf{h}, k)}{\|\mathbf{h} - \boldsymbol{\mu}_{\text{train}}\|_2}$. The regularizer compares ID/OOD at equal deviation levels, empirically sharpening separation; the distance term captures that ID features tend to reside farther from decision boundaries than OOD features.

A.2.8 predictive Normalized Maximum Likelihood (pNML) (Bibas et al., 2021)

pNML treats a deep network as a fixed feature extractor and for each test samples computes a regret score by simulating in closed form the best last-layer update for every possible label. Given the matrix of normalized penultimate-layer training activations $\hat{\mathbf{H}} = [\mathbf{h}_1/\|\mathbf{h}_1\|_2, \dots, \mathbf{h}_N/\|\mathbf{h}_N\|_2]$, the online-update direction \mathbf{g} via the kernel-range projection is $\mathbf{g} = \mathbf{h}_\perp/\|\mathbf{h}_\perp\|_2^2$ if $\mathbf{h}_\perp = (\mathbf{I} - \hat{\mathbf{H}}^\top \hat{\mathbf{H}})\mathbf{h} \neq 0$; else $\mathbf{g} = \frac{\hat{\mathbf{H}}^\top \hat{\mathbf{H}}^\top \mathbf{h}}{1 + \mathbf{h}^\top \hat{\mathbf{H}}^\top \hat{\mathbf{H}}^\top \mathbf{h}}$, where $\hat{\mathbf{H}}^\top$ is the Moore–Penrose inverse of the normalized training activations. The pNML regret is $\text{pNML}(\mathbf{x}) = \log \sum_{k=1}^C \frac{\mathbf{p}_k}{\mathbf{p}_k + \mathbf{p}_k^\top \mathbf{g} (1 - \mathbf{p}_k)}$ and serves as an OOD/failure score (larger pNML \Rightarrow less trustworthy prediction). Intuitively, pNML is small when \mathbf{h} lies in the high-variance ID subspace or is far from decision boundaries (the genie’s label-specific update has little effect), and large otherwise.

A.2.9 GradNorm (Huang et al., 2021)

Given a trained classifier with softmax $p(\mathbf{x})$, GradNorm defines the OOD score as the vector norm of the gradients obtained by backpropagating the Kullback–Leibler divergence from a *uniform* target, i.e. $\text{GradNorm}(\mathbf{x}) = \|\partial_w \text{KL}(\mathbf{u} \| p(\mathbf{x}))\|_p = \left\| \frac{1}{C} \sum_{k=1}^C \frac{\partial \mathcal{L}_{\text{CE}}(g(\mathbf{h}), k)}{\partial \mathbf{w}} \right\|_p$, typically using the L_1 norm on the *last-layer* weights. This choice is label-agnostic and exploits that in-distribution inputs produce more *peaked* predictions and thus larger gradients than OOD inputs. A simple analysis shows $\text{GradNorm}(\mathbf{x})$ factorizes into a feature-space term and an output-space term, capturing joint information that improves separability over output-only scores.

A.2.10 PCA Reconstruction Error (PCA RecError) (Guan et al., 2023)

PCA Reconstruction Error models the in-distribution feature manifold by fitting a low-dimensional principal subspace on penultimate features and scores a test example by the energy of its component orthogonal to that subspace, so larger residuals indicate atypicality. This approach computes the ID mean $\boldsymbol{\mu}$ and covariance $\boldsymbol{\Sigma}$, then takes the top- k eigenvectors \mathbf{U}_k of $\boldsymbol{\Sigma}$, and forms the projector $\mathbf{M} = \mathbf{U}_k \mathbf{U}_k^\top$. The *PCA reconstruction error* for a test point is $e(\mathbf{x}) = \|(\mathbf{I} - \mathbf{M})(\mathbf{h}(\mathbf{x}) - \boldsymbol{\mu})\|_2$, i.e., the energy of the component orthogonal to the ID principal subspace. Although intuitively $e(\mathbf{x})$ should be smaller on ID than OOD, a detailed analysis shows that $e(\mathbf{x})$ (i) mixes the angle between $\mathbf{h}(\mathbf{x}) - \boldsymbol{\mu}$ and the principal subspace and (ii) the norm $\|\mathbf{h}(\mathbf{x}) - \boldsymbol{\mu}\|_2$, which is typically *larger* for ID than OOD; this blurs separability for vanilla PCA-OOD. To mitigate the norm effect, a simple regularized score $r(\mathbf{x}) = \frac{\|\mathbf{h} - \hat{\mathbf{h}}\|_2}{\|\mathbf{h}\|_2}$, where $\hat{\mathbf{h}} = \hat{\mathbf{h}}(\mathbf{x}) = \mathbf{M}(\mathbf{h}(\mathbf{x}) - \boldsymbol{\mu}) + \boldsymbol{\mu}$, improves discrimination, and can be fused multiplicatively with logit-based scores.

A.2.11 Kernel PCA Reconstruction Error (KPCA RecError) (Fang et al., 2025)

KPCA Reconstruction Error models the in-distribution (ID) feature manifold in a *non-linear* subspace and scores a test point by its reconstruction error in that subspace. To mitigate feature–norm imbalance and preserve useful Euclidean relations, KPCA first ℓ_2 –normalizes features $\hat{\mathbf{h}} = \mathbf{h}/\|\mathbf{h}\|_2$ and define a Gaussian kernel on the unit sphere $k(\mathbf{x}, \mathbf{x}') = \exp\left(-\frac{1}{2\sigma^2} \|\hat{\mathbf{h}} - \hat{\mathbf{h}}'\|_2^2\right) = \exp\left(-\frac{1}{\sigma^2} (1 - \cos(\hat{\mathbf{h}}, \hat{\mathbf{h}}'))\right)$, which can be viewed as a Cosine–Gaussian composition. Given ID training points, the centered Gram matrix is defined as $\mathbf{K}_c = \mathbf{H} \mathbf{K} \mathbf{H}$ with $\mathbf{K}_{ij} = k(\mathbf{x}_i, \mathbf{x}_j)$ and $\mathbf{H} = \mathbf{I} - \frac{1}{n} \mathbf{1} \mathbf{1}^\top$. Using the centered Gram matrix, KPCA solves the eigenproblem $\mathbf{K}_c \boldsymbol{\alpha}_m = n \lambda_m \boldsymbol{\alpha}_m$, where $m = 1, \dots, N$, and defines principal coordinates for a test point \mathbf{x} via the centered kernel $k_c(\mathbf{x}, \mathbf{x}_i) = k(\mathbf{x}, \mathbf{x}_i) - \frac{1}{n} \sum_j k(\mathbf{x}, \mathbf{x}_j) - \frac{1}{n} \sum_j k(\mathbf{x}_j, \mathbf{x}_i) + \frac{1}{n^2} \sum_{j \neq i} k(\mathbf{x}_j, \mathbf{x}_i)$: $\phi_m(\mathbf{x}) = \frac{1}{\sqrt{\lambda_m}} \sum_{i=1}^N \boldsymbol{\alpha}_{mi} k_c(\mathbf{x}, \mathbf{x}_i)$. The squared reconstruction error in feature space after projecting onto the top k components is $e(\mathbf{x}) = k_c(\mathbf{x}, \mathbf{x}) - \sum_{m=1}^k \phi_m(\mathbf{x})^2$. Similar to PCA Reconstruction Error, the larger $e(\mathbf{x})$ is, the more atypical \mathbf{x} becomes. A norm–regularized variant $\text{KPCA}(\mathbf{x}) = e(\mathbf{x})/\sqrt{k_c(\mathbf{x}, \mathbf{x})}$ further reduces residual norm confounds.

To avoid computing the full $N \times N$ kernel and $O(N^2)$ memory, we approximate the Gaussian on the sphere with an explicit map $\psi : \mathbb{R}^D \rightarrow \mathbb{R}^M$ so that $k(\mathbf{x}, \mathbf{x}') \approx \psi(\hat{\mathbf{h}})^\top \psi(\hat{\mathbf{h}}')$ with $M \ll N$. In particular, we use Nyström features with landmarks $\{\mathbf{x}_\ell^*\}_{\ell=1}^M$ (e.g., low-energy ID points near the boundary), $\psi(\tilde{\mathbf{z}}) = C W^{-1/2}$ where $C_\ell = k(\mathbf{x}, \mathbf{x}_\ell^*)$ and W is the landmark Gram matrix. We then perform ordinary PCA on $\psi(\hat{\mathbf{h}})$: compute mean $\boldsymbol{\mu}$ and top- k eigenvectors \mathbf{U}_k of the empirical covariance, and score a test point by the Euclidean reconstruction error $\tilde{e}(\mathbf{x}) = \|(\mathbf{I} - \mathbf{U}_k \mathbf{U}_k^\top)(\psi(\hat{\mathbf{h}}) - \boldsymbol{\mu})\|_2^2$, and $\tilde{r}(\mathbf{x}) = \frac{\tilde{e}(\mathbf{x})}{\|\psi(\hat{\mathbf{h}})\|_2}$. Empirically, the Cosine–Gaussian kernel and the

low-energy Nyström approximation improve separability and efficiency over linear PCA and nearest-neighbor baselines.

A.2.12 Residual Projection and Virtual Matching Logit (ViM) (Wang et al., 2022)

Residual Projection score. If the ID principal subspace $P \subset \mathbb{R}^N$ from training features is defined as the span of the top- D eigenvectors of $\mathbf{H}^\top \mathbf{H}$, then $R \in \mathbb{R}^{N \times (N-D)}$ have columns spanning P^\perp . The *residual* projection of \mathbf{x} is $r(\mathbf{x}) = RR^\top \mathbf{h}$, and the residual projection score is $\text{Residual}(\mathbf{x}) = \|r(\mathbf{x})\|_2$, which increases as the feature departs from the ID principal subspace. This score is class-agnostic and leverages feature-space geometry that is lost when projecting to logits.

ViM (Virtual-logit Matching). ViM fuses the class-agnostic residual with class-dependent logits by creating a virtual $(K+1)$ -st logit from the residual and matching its scale to the real logits. ViM score is defined as the softmax probability of this virtual class: $\text{ViM}(\mathbf{x}) = \frac{\exp\{\ell_0(\mathbf{x})\}}{\sum_{k=1}^K \exp\{g(\mathbf{x})_k\} + \exp\{\ell_0(\mathbf{x})\}}$, where the virtual logit $\ell_0(\mathbf{x}) = \alpha \|r(\mathbf{x})\|_2$, and the scaling factor $\alpha = \mathbb{E}_{\mathbf{x} \sim \text{ID}}[\max_{k \leq K} f_k(\mathbf{x})]/\mathbb{E}_{\mathbf{x} \sim \text{ID}}[\|r(\mathbf{x})\|_2]$. Equivalently, applying the transformation $t(x) = -\ln(1/x - 1)$ yields $t(\text{ViM}(\mathbf{x})) = \alpha \|r(\mathbf{x})\|_2 - \log \sum_{k=1}^K e^{g(\mathbf{x})_k}$, i.e., a residual term minus the *Energy* of the logits. Thus ViM is large when the residual is large and the (ID) logits are small.

A.2.13 Neural Collapse (NeCo) (Ammar et al., 2023)

This method is motivated by the Neural Collapse phenomena (Papyan et al., 2020), which unveils geometric properties that manifest at the end of the training process. NeCo's new observation establishes ID/OOD orthogonality, which implies that OOD features concentrate near the origin after projection onto the ID subspace. This method fits PCA on ID features to obtain the top- d principal directions $\mathbf{P} \in \mathbb{R}^{D \times d}$ (orthonormal columns). Then it scores an input by the normalized projection of its feature onto the ID principal subspace, $\text{NeCo}(\mathbf{x}) = \frac{\|\mathbf{P}^\top \mathbf{h}\|_2}{\|\mathbf{h}\|_2}$, so that ID points (well aligned with the ID subspace) yield larger scores, while OOD points (near-orthogonal to that subspace) yield smaller scores. This score is optionally calibrated by multiplying with MLS to inject class-scale information.

A.3 Methods Variations

As described in section 3.2, the global and class subspaces, \mathbf{P} and \mathbf{P}^c respectively, allow multiple projections that can be used to modify existing OOD detection methods. The following list shows possible modifications to the feature, logit and probability spaces, and table 3:

- **Global projection:** $\hat{\mathbf{h}} = \mathbf{P}\mathbf{P}^\top(\mathbf{h} - \boldsymbol{\mu}_{\text{train}}) + \boldsymbol{\mu}_{\text{train}}$
- **Class projection:** $\hat{\mathbf{h}}^c = \mathbf{P}^c\mathbf{P}^{c\top}(\mathbf{h} - \boldsymbol{\mu}_{\text{train}}^c) + \boldsymbol{\mu}_{\text{train}}^c$
- **Class averaged projection:** $\hat{\mathbf{h}}^{\text{avg}} = \frac{1}{C} \sum_{c=1}^C \hat{\mathbf{h}}^c$
- **Class predicted projection:** $\hat{\mathbf{h}}^{\text{pred}} = \hat{\mathbf{h}}^{\hat{y}}$, where $\hat{y} = m(\mathbf{x})$
- **Class projected logit:** $\hat{g}^{\text{class}} = [\hat{g}^1, \dots, \hat{g}^C]$, where $\hat{g}^c = \mathbf{w}_{cL}^\top \hat{\mathbf{h}}^c + b_{cL}$
- **Global projected probabilities:** $\hat{\mathbf{p}} = \left[\frac{\exp(g(\hat{\mathbf{h}})_1)}{\sum_j \exp(g(\hat{\mathbf{h}})_j)}, \dots, \frac{\exp(g(\hat{\mathbf{h}})_C)}{\sum_j \exp(g(\hat{\mathbf{h}})_j)} \right]$
- **Class projected probabilities:** $\hat{\mathbf{p}}^{\text{class}} = \left[\frac{\exp(\hat{g}^1)}{\sum_j \exp(\hat{g}^j)}, \dots, \frac{\exp(\hat{g}^C)}{\sum_j \exp(\hat{g}^j)} \right]$
- **Class-predicted probabilities:** $\hat{\mathbf{p}}^{\text{pred}} = \left[\frac{\exp(g(\hat{\mathbf{h}}^{\text{pred}})_1)}{\sum_j \exp(g(\hat{\mathbf{h}}^{\text{pred}})_j)}, \dots, \frac{\exp(g(\hat{\mathbf{h}}^{\text{pred}})_C)}{\sum_j \exp(g(\hat{\mathbf{h}}^{\text{pred}})_j)} \right]$
- **Class-averaged probabilities:** $\hat{\mathbf{p}}^{\text{avg}} = \left[\frac{\exp(g(\hat{\mathbf{h}}^{\text{avg}})_1)}{\sum_j \exp(g(\hat{\mathbf{h}}^{\text{avg}})_j)}, \dots, \frac{\exp(g(\hat{\mathbf{h}}^{\text{avg}})_C)}{\sum_j \exp(g(\hat{\mathbf{h}}^{\text{avg}})_j)} \right]$

Table 3: OOD Detection methods baselines and variations. This table synthesizes multiple variations using our proposed Projection Filtering approach for all the OOD detection methods considered in this work.

Score	Unmodified	Global	Class	Class Pred	Class Avg
CTM	$\max_k \text{sim}(\mathbf{w}_k, \mathbf{h})$	$\max_k \text{sim}(\mathbf{w}_k, \hat{\mathbf{h}})$	$\max_k \text{sim}(\mathbf{w}_k, \hat{\mathbf{h}}^k)$	$\max_k \text{sim}(\mathbf{w}_k, \hat{\mathbf{h}}_{\text{pred}})$	$\max_k \text{sim}(\mathbf{w}_k, \hat{\mathbf{h}}^{\text{avg}})$
CTM(mean)	$\max_k \text{sim}(\boldsymbol{\mu}_k, \mathbf{h})$	$\max_k \text{sim}(\boldsymbol{\mu}_k, \hat{\mathbf{h}})$	$\max_k \text{sim}(\boldsymbol{\mu}_k, \hat{\mathbf{h}}^k)$	$\max_k \text{sim}(\boldsymbol{\mu}_k, \hat{\mathbf{h}}_{\text{pred}})$	$\max_k \text{sim}(\boldsymbol{\mu}_k, \hat{\mathbf{h}}^{\text{avg}})$
Energy	$-T \log \sum_{k=1}^C e^{g(\mathbf{h})_k/T}$	$-T \log \sum_{k=1}^C e^{g(\hat{\mathbf{h}})_k/T}$	$-T \log \sum_{k=1}^C e^{\hat{g}_{\text{class}}}$	$-T \log \sum_{k=1}^C e^{g(\hat{\mathbf{h}}_{\text{pred}})_k/T}$	$-T \log \sum_{k=1}^C e^{g(\hat{\mathbf{h}}^{\text{avg}})_k/T}$
MSR	$\max_k \mathbf{p}_k$	$\max_k \hat{\mathbf{p}}_k$	$\max_k \hat{\mathbf{p}}_{\text{class}}$	$\max_k \hat{\mathbf{p}}_{\text{pred}}$	$\max_k \hat{\mathbf{p}}^{\text{avg}}$
MLS	$\max_k g(\mathbf{h})_k$	$\max_k g(\hat{\mathbf{h}})_k$	$\max_k g(\hat{\mathbf{h}}_{\text{class}})$	$\max_k g(\hat{\mathbf{h}}_{\text{pred}})_k$	$\max_k g(\hat{\mathbf{h}}^{\text{avg}})_k$
PE	$\sum_{k=1}^C \mathbf{p}_k \log \mathbf{p}_k$	$\sum_{k=1}^C \hat{\mathbf{p}}_k \log \hat{\mathbf{p}}_k$	$\sum_{k=1}^C (\hat{\mathbf{p}}_{\text{class}}^{\text{class}}) \log (\hat{\mathbf{p}}_{\text{class}}^{\text{class}})$	$\sum_{k=1}^C (\hat{\mathbf{p}}_{\text{pred}}^{\text{pred}}) \log (\hat{\mathbf{p}}_{\text{pred}}^{\text{pred}})$	$\sum_{k=1}^C (\hat{\mathbf{p}}_k^{\text{avg}}) \log (\hat{\mathbf{p}}_k^{\text{avg}})$
GEN	$\sum_{k=1}^M \mathbf{p}_k^\gamma (1 - \mathbf{p}_k^\gamma)$	$\sum_{k=1}^M \hat{\mathbf{p}}_k^\gamma (1 - \hat{\mathbf{p}}_k^\gamma)$	$\sum_{k=1}^M (\hat{\mathbf{p}}_k^{\text{class}})^\gamma [1 - (\hat{\mathbf{p}}_k^{\text{class}})^\gamma]$	$\sum_{k=1}^M (\hat{\mathbf{p}}_k^{\text{pred}})^\gamma [1 - (\hat{\mathbf{p}}_k^{\text{pred}})^\gamma]$	$\sum_{k=1}^M (\hat{\mathbf{p}}_k^{\text{avg}})^\gamma [1 - (\hat{\mathbf{p}}_k^{\text{avg}})^\gamma]$
REN	$\frac{1}{1-\gamma} \log \sum_{k=1}^M \mathbf{p}_k^\gamma$	$\frac{1}{1-\gamma} \log \sum_{k=1}^M \hat{\mathbf{p}}_k^\gamma$	$\frac{1}{1-\gamma} \log \sum_{k=1}^M (\hat{\mathbf{p}}_k^{\text{class}})^\gamma$	$\frac{1}{1-\gamma} \log \sum_{k=1}^M (\hat{\mathbf{p}}_k^{\text{pred}})^\gamma$	$\frac{1}{1-\gamma} \log \sum_{k=1}^M (\hat{\mathbf{p}}_k^{\text{avg}})^\gamma$
GE	$\sum_{k=1}^C k \mathbf{p}_{(k)}$	$\sum_{k=1}^C k \hat{\mathbf{p}}_{(k)}$	$\sum_{k=1}^C k \mathbf{p}_{(k)}^{\text{class}}$	$\sum_{k=1}^C k \hat{\mathbf{p}}_{(k)}^{\text{pred}}$	$\sum_{k=1}^C k \hat{\mathbf{p}}_{(k)}^{\text{avg}}$
PCE	$-\log \sum_{k=1}^C \mathbf{p}_k^2$	$-\log \sum_{k=1}^C \hat{\mathbf{p}}_k^2$	$-\log \sum_{k=1}^C (\hat{\mathbf{p}}_k^{\text{class}})^2$	$-\log \sum_{k=1}^C (\hat{\mathbf{p}}_k^{\text{pred}})^2$	$-\log \sum_{k=1}^C (\hat{\mathbf{p}}_k^{\text{avg}})^2$
Malta	$\max_k \bar{\mathbf{h}}_k^\top \Sigma^{-1} \bar{\mathbf{h}}_k$	$\max_k \bar{\hat{\mathbf{h}}}_k^\top \Sigma^{-1} \bar{\hat{\mathbf{h}}}_k$	$\max_k (\bar{\hat{\mathbf{h}}}_k^{\text{pred}})_k^\top (\bar{\Sigma}^{\text{pred}})^{-1} (\bar{\hat{\mathbf{h}}}_k^{\text{pred}})_k$	$\max_k (\bar{\hat{\mathbf{h}}}_k^{\text{avg}})_k^\top (\bar{\Sigma}^{\text{avg}})^{-1} (\bar{\hat{\mathbf{h}}}_k^{\text{avg}})_k$	
NNGuide	$E(\mathbf{h})G(\mathbf{h})$	$E(\hat{\mathbf{h}})G(\hat{\mathbf{h}})$	$E(\mathbf{h}^{\text{pred}})G(\mathbf{h}^{\text{pred}})$	$E(\mathbf{h}^{\text{avg}})G(\mathbf{h}^{\text{avg}})$	
fDBD	$\frac{1}{C-1} \sum_{k=1}^C \sum_{k \neq m(\mathbf{x})} \frac{D_g(\mathbf{h}_k, k)}{\ \mathbf{h}_k - \mathbf{h}_{\text{train}}\ }$	$\frac{1}{C-1} \sum_{k=1}^C \sum_{k \neq m(\mathbf{x})} \frac{D_g(\hat{\mathbf{h}}_k, k)}{\ \hat{\mathbf{h}}_k - \hat{\mathbf{h}}_{\text{train}}\ }$	$\frac{1}{C-1} \sum_{k=1}^C \sum_{k \neq m(\mathbf{x})} \frac{D_g(\hat{\mathbf{h}}_{\text{pred}}_k, k)}{\ \hat{\mathbf{h}}_{\text{pred}}_k - \hat{\mathbf{h}}_{\text{train}}\ }$	$\frac{1}{C-1} \sum_{k=1}^C \sum_{k \neq m(\mathbf{x})} \frac{D_g(\hat{\mathbf{h}}_{\text{avg}}_k, k)}{\ \hat{\mathbf{h}}_{\text{avg}}_k - \hat{\mathbf{h}}_{\text{train}}\ }$	
pNML	$\log \sum_{k=1}^C \frac{\mathbf{p}_k + \mathbf{p}_k^\top \mathbf{y} (1 - \mathbf{p}_k)}{\mathbf{p}_k + \hat{\mathbf{p}}_k^\top \mathbf{y} (1 - \mathbf{p}_k)}$	$\log \sum_{k=1}^C \frac{\hat{\mathbf{p}}_k + \hat{\mathbf{p}}_k^\top \mathbf{y} (1 - \mathbf{p}_k)}{\hat{\mathbf{p}}_k + \hat{\mathbf{p}}_k^\top \mathbf{y} (1 - \mathbf{p}_k)}$	$\log \sum_{k=1}^C \frac{\hat{\mathbf{p}}_{\text{pred}} + (\hat{\mathbf{p}}_k^{\text{pred}})^\top \mathbf{y} (1 - \hat{\mathbf{p}}_{\text{pred}})}{\hat{\mathbf{p}}_k^{\text{pred}} + (\hat{\mathbf{p}}_k^{\text{pred}})^\top \mathbf{y} (1 - \hat{\mathbf{p}}_{\text{pred}})}$	$\log \sum_{k=1}^C \frac{\hat{\mathbf{p}}_{\text{avg}} + (\hat{\mathbf{p}}_k^{\text{avg}})^\top \mathbf{y} (1 - \hat{\mathbf{p}}_{\text{avg}})}{\hat{\mathbf{p}}_k^{\text{avg}} + (\hat{\mathbf{p}}_k^{\text{avg}})^\top \mathbf{y} (1 - \hat{\mathbf{p}}_{\text{avg}})}$	
GradNorm	$\left\ \frac{1}{C} \sum_{k=1}^C \frac{\partial \mathcal{L}_{\text{CE}}(g(\mathbf{h}), k)}{\partial \mathbf{w}} \right\ $	$\left\ \frac{1}{C} \sum_{k=1}^C \frac{\partial \mathcal{L}_{\text{CE}}(g(\hat{\mathbf{h}}), k)}{\partial \mathbf{w}} \right\ $	$\left\ \frac{1}{C} \sum_{k=1}^C \frac{\partial \mathcal{L}_{\text{CE}}(g(\hat{\mathbf{h}}^{\text{pred}}), k)}{\partial \mathbf{w}} \right\ $	$\left\ \frac{1}{C} \sum_{k=1}^C \frac{\partial \mathcal{L}_{\text{CE}}(g(\hat{\mathbf{h}}^{\text{avg}}), k)}{\partial \mathbf{w}} \right\ $	
PCA Error	$-\frac{\ \mathbf{h} - \hat{\mathbf{h}}\ }{\ \mathbf{h}\ }$	$\max_k -\frac{\ \mathbf{h} - \hat{\mathbf{h}}_k\ }{\ \mathbf{h}\ }$	$\max_k -\frac{\ \mathbf{h} - \hat{\mathbf{h}}_{\text{pred}}\ }{\ \mathbf{h}\ }$		
ViM	$\alpha \ \hat{\mathbf{R}}\mathbf{h}\ + E(\mathbf{h})$				
NeCo		$\frac{\ \hat{\mathbf{P}}\mathbf{h}\ }{\ \mathbf{h}\ }$			
Residual		$\ \hat{\mathbf{R}}\mathbf{h}\ $			
Confidence		$s_{\mathcal{W}}$			

B CLIP-based OOD Aggregation

Let ϕ_{img} and ϕ_{text} be fixed CLIP encoders (Radford et al., 2021). For any image \mathbf{x} , define the ℓ_2 -normalized image embedding $z = \tilde{\phi}_{\text{img}}(\mathbf{x}) = \phi_{\text{img}}(\mathbf{x}) / \|\phi_{\text{img}}(\mathbf{x})\|_2 \in \mathbb{R}^d$. Given an in-distribution set $\mathcal{D}_{\text{ID}} = \{\mathbf{x}_i, y_i\}_{i=1}^N$ and a candidate OOD set $\mathcal{D}_{\text{OOD}} = \{\mathbf{x}'_j\}_{j=1}^m$, we extract $Z_{\text{train}} = \{\mathbf{z}_i\}_{i=1}^n$ and $Z_{\text{OOD}} = \{\mathbf{z}'_j\}_{j=1}^m$ under identical preprocessing.

Global distances. We summarize each set by its empirical Gaussian in CLIP space with means and covariances $(\boldsymbol{\mu}_{\text{ID}}, \boldsymbol{\Sigma}_{\text{ID}})$ and $(\boldsymbol{\mu}_{\text{OOD}}, \boldsymbol{\Sigma}_{\text{OOD}})$, and compute the Fréchet distance (FD) (Dowson and Landau, 1982; Fréchet, 1957): $\text{FD}^2(\mathcal{D}_{\text{OOD}} \rightarrow \mathcal{D}_{\text{ID}}) = \|\boldsymbol{\mu}_{\text{ID}} - \boldsymbol{\mu}_{\text{OOD}}\|_2^2 + \text{Tr}(\boldsymbol{\Sigma}_{\text{ID}} + \boldsymbol{\Sigma}_{\text{OOD}} - 2(\boldsymbol{\Sigma}_{\text{ID}}^{1/2} \boldsymbol{\Sigma}_{\text{OOD}} \boldsymbol{\Sigma}_{\text{ID}}^{1/2})^{1/2})$.

As a second global measure, we compute the (unbiased) maximum mean discrepancy (MMD) (Gretton et al., 2006) with a polynomial kernel $k(\mathbf{u}, \mathbf{v}) = (\mathbf{u}^\top \mathbf{v} + c)^d$: $\widehat{\text{MMD}}^2 = \frac{1}{n(n-1)} \sum_{i \neq i'} k(\mathbf{z}_i, \mathbf{z}_{i'}) + \frac{1}{m(m-1)} \sum_{j \neq j'} k(\mathbf{z}'_j, \mathbf{z}'_{j'}) - \frac{2}{nm} \sum_{i,j} k(\mathbf{z}_i, \mathbf{z}'_j)$. Both quantities are evaluated on CLIP embeddings; *smaller* values indicate that \mathcal{D}_{OOD} is closer to the ID manifold.

Class-aware distances. For ID class $c \in \{1, \dots, K\}$, define the (normalized) image-prototype $\boldsymbol{\mu}_c = (\frac{1}{|\mathcal{D}_c|} \sum_{i:y_i=c} \mathbf{z}_i) / \|\frac{1}{|\mathcal{D}_c|} \sum_{i:y_i=c} \mathbf{z}_i\|_2$ and the (normalized) text prototype $\mathbf{t}_c = (\frac{1}{L} \sum_{\ell=1}^L \phi_{\text{text}}(\text{prompt}_\ell(c))) / \|\frac{1}{L} \sum_{\ell=1}^L \phi_{\text{text}}(\text{prompt}_\ell(c))\|_2$ (using prompt ensembling for class c). For a test embedding \mathbf{z}' , define the nearest-centroid cosine distance $d_{\text{NC}}(\mathbf{z}') = 1 - \max_{c \leq K} \mathbf{z}'^\top \boldsymbol{\mu}_c$, and the image–text cosine distance $d_{\text{IT}}(\mathbf{z}') = 1 - \max_{c \leq K} \mathbf{z}'^\top \mathbf{t}_c$. Aggregate per-dataset by averaging: $\bar{d}_{\text{NC}} = \frac{1}{m} \sum_{j=1}^m d_{\text{NC}}(\mathbf{z}'_j)$ and $\bar{d}_{\text{IT}} = \frac{1}{m} \sum_{j=1}^m d_{\text{IT}}(\mathbf{z}'_j)$. Lower values mean the OOD set is *class-closer* to ID.

Clustering into proximity buckets. We orient all four metrics so that lower \Rightarrow closer and form a feature vector $\mathbf{v}(\mathcal{D}_{\text{OOD}}) = [\text{FD}^2, \widehat{\text{MMD}}^2, \bar{d}_{\text{NC}}, \bar{d}_{\text{IT}}]^\top$. We standardize \mathbf{v} across candidate OOD sets (z-score per coordinate) and run k -means with $k = 3$ (fixed seed) to obtain proximity buckets labeled *near/mid/far*. This CLIP-based protocol is detector-agnostic and applies unchanged to any ID label space or downstream OOD scoring rule.

C Statistical Tests for Clique Generation

Let k be the number of CSFs and N the number of complete blocks (e.g., each block is a dataset/condition on which all k methods are evaluated on the same metric). Within block $i \in \{1, \dots, N\}$, rank the methods so that $r_{ij} \in \{1, \dots, k\}$ is the rank of method j (use mid-ranks for ties). Define the average rank $\bar{R}_j = \frac{1}{N} \sum_{i=1}^N r_{ij}$. The Friedman statistic tests the null H_0 : all methods are equivalent in distribution of ranks (Fréchet, 1957; Demšar, 2006):

$$Q = \frac{12N}{k(k+1)} \sum_{j=1}^k \bar{R}_j^2 - 3N(k+1),$$

(optionally applying a standard tie correction within blocks). For finite samples, the Iman–Davenport F -approximation is recommended (Iman and Davenport, 1980):

$$F_F = \frac{(N-1)Q}{N(k-1) - Q} \sim F_{k-1, (k-1)(N-1)}.$$

If F_F exceeds the critical value at level α , we reject H_0 and proceed with post-hoc pairwise comparisons.

Conover post-hoc & Bron–Kerbosch cliques (top groups). For each pair (i, j) we compare average ranks using Conover's post-hoc test (Conover, 1999). With common standard error

$$\text{SE} = \sqrt{\frac{k(k+1)}{6N}}, \quad T_{ij} = \frac{|\bar{R}_i - \bar{R}_j|}{\text{SE}},$$

two-sided p -values are obtained from the normal (or t) reference, and multiplicity is controlled across all $\binom{k}{2}$ pairs using Holm's step-down procedure (Holm, 1979). To summarize statistically indistinguishable winners, construct an *indifference graph* $G = (V, E)$ with nodes $V = \{1, \dots, k\}$ (methods) and edges $(i, j) \in E$ iff the

(a) CLIP-based distance metrics. Dataset: CIFAR-10						
	Kernel MMD	Global	FD	Label-Text Alignment	Class-aware	Image Centroid Distance
Test	-0.0000	0.0028	0.7183	0.6349	ID	
CIFAR-100	0.0002	0.1592	0.7885	0.8085	Near	Test
TinyImagenet	0.0009	0.3233	0.8060	0.9256	Near	CIFAR-10
iSUN	0.0015	0.4890	0.7943	0.8393	Mid	0.0000
LSUN resize	0.0016	0.5248	0.8045	0.8634	Mid	0.0002
LSUN cropped	0.0015	0.5129	0.7797	0.8168	Mid	0.1705
SVHN	0.0020	0.709	0.7744	0.8607	Mid	0.7701
Places 365	0.0021	0.6379	0.8337	1.1471	Far	0.7511
Textures	0.0020	0.6698	0.8231	1.0647	Far	0.8738

(c) CLIP-based distance metrics. Dataset: CIFAR-100						
	Kernel MMD	Global	FD	Label-Text Alignment	Class-aware	Image Centroid Distance
Test	-0.0000	0.0033	0.7043	0.6026	ID	
CIFAR-10	0.0002	0.1590	0.7494	0.7268	Near	Test
TinyImagenet	0.0008	0.2235	0.7512	0.8436	Near	CIFAR-100
iSUN	0.0012	0.3829	0.7484	0.7128	Mid	0.0008
LSUN resize	0.0013	0.4204	0.7562	0.7388	Mid	0.2224
LSUN cropped	0.0011	0.3999	0.7364	0.7120	Mid	0.3220
SVHN	0.0017	0.6222	0.7511	0.7789	Mid	iSUN
Places 365	0.0019	0.5456	0.7752	1.0568	Far	0.0012
Textures	0.0016	0.5232	0.7613	0.9780	Far	0.3808

(b) CLIP-based distance metrics. Dataset: SuperCIFAR-100						
	Kernel MMD	Global	FD	Label-Text Alignment	Class-aware	Image Centroid Distance
Test	0.0000	0.0748	0.7581	0.7031	ID	
CIFAR-10	0.0002	0.1705	0.7701	0.7511	Near	Test
TinyImagenet	0.0008	0.2307	0.7840	0.8738	Near	CIFAR-10
iSUN	0.0012	0.3856	0.7607	0.7425	Mid	0.0000
LSUN resize	0.0013	0.4244	0.7625	0.7720	Mid	0.0002
LSUN cropped	0.0011	0.3999	0.7696	0.7351	Mid	0.1705
SVHN	0.0017	0.6208	0.7566	0.8012	Mid	0.7701
Places 365	0.0020	0.5562	0.7939	1.0964	Far	0.7511
Textures	0.0016	0.5246	0.7980	1.0003	Far	0.8738

(d) CLIP-based distance metrics. Dataset: TinyImagenet						
	Kernel MMD	Global	FD	Label-Text Alignment	Class-aware	Image Centroid Distance
Test	-0.0000	0.0036	0.7141	0.6319	ID	
CIFAR-100	0.0008	0.2224	0.7279	0.7956	Near	Test
CIFAR-10	0.0009	0.3220	0.7288	0.7979	Near	CIFAR-100
iSUN	0.0012	0.3808	0.7468	0.7063	Mid	0.0008
LSUN resize	0.0013	0.4039	0.7500	0.7186	Mid	0.2224
LSUN cropped	0.0016	0.4989	0.7406	0.7503	Mid	0.3220
Places 365	0.0014	0.3887	0.7645	0.9846	Mid	iSUN
Textures	0.0014	0.4697	0.7528	0.9317	Mid	0.0012
SVHN	0.0025	0.7948	0.7409	0.8726	Far	0.3808

adjusted $p_{ij} \geq \alpha$ (i.e., the pair is not significantly different). Enumerate all *maximal cliques* of G using the Bron–Kerbosch algorithm with pivoting (state (R, P, X) ; recursively add $v \in P \setminus N(u)$ for a high-degree pivot u ; output R when $P = X = \emptyset$) (Bron and Kerbosch, 1973). Each maximal clique is a set of methods that are mutually indistinguishable under Conover–Holm; reporting the leading clique(s)—sorted by best/mean \bar{R} —yields layered, statistically justified “top groups,” alongside \bar{R}_j and the full adjusted p -matrix for transparency.